J. Fluid Mech. (2022), *vol*. 951, A22, doi:10.1017/jfm.2022.829

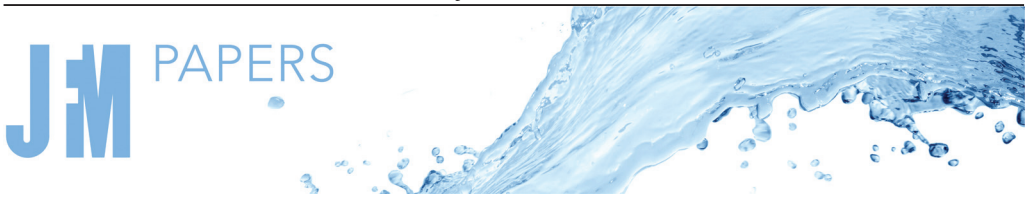

Dispersion of a passive scalar around a Taylor bubble

D. Picchi[1],† **and P. Poesio**[1]

[1]Department of Mechanical and Industrial Engineering, Università degli Studi di Brescia, Brescia 25123, Italy

(Received 22 April 2022; revised 28 September 2022; accepted 28 September 2022)

The motion of Taylor bubbles in capillaries is typical of many engineering and biological systems, ranging from subsurface flows to small-scale reactors. Although the hydrodynamics of elongated bubbles has been the object of several studies, the case where a solute is transported in the surrounding liquid and surface mass-transfer mechanisms act on the solid wall or the bubble–fluid interface is much less understood. To fill this gap, we investigate the transport problem around a confined Taylor bubble to access the competition between advection, diffusion and surface mass transfer in the different regions of the bubble. With this aim, we derive a one-dimensional advection–diffusion–mass-transfer equation where the transport mechanisms are described through an effective velocity, an effective diffusion coefficient and an effective Sherwood number. Our model generalises the Aris–Taylor dispersion to the case of a Taylor bubble and clarifies the impact of surface mass transfer in the advection and diffusion dominated regimes for both the front and rear menisci. The model recovers the typical Pèclet square relationship of the effective diffusion coefficient, which also depends on the film thickness. Also, when the Pèclet number balances with the Sherwood number, there exist conditions that lead to the formation of hot spots of concentration. We show that the typical shape oscillations of the bubble rear locally enhance superficial mass transfer. Finally, we study the transport problem in the uniform film region where the concentration field can be found analytically.

Key words: bubble dynamics, dispersion, reacting multiphase flow

† Email address for correspondence: davide.picchi@unibs.it

1. Introduction

The study of mass transfer in confined geometries is extremely important in many engineering and biological systems. In the context of geological CO_2 sequestration, carbon dioxide is injected into subsurface reservoirs, leading to the formation of elongated bubbles that can either be trapped, move or interact with the solid matrix (e.g. Rathnaweera, Ranjith & Perera 2016; Soulaine *et al.* 2018; Li, Garing & Benson 2020). The presence of CO_2 has the effect of increasing the acidity of the *in situ* brine, boosting a series of chain reactions that enhance rock dissolution (Steefel, Molins & Trebotich 2013). This may threaten the long-term integrity of the storage process due to the formation of leakage pathways for carbon dioxide.

In medicine, a good understanding of the coupling between the hydrodynamics of confined bubbles and mass transfer is fundamental for treating air embolism (e.g. Grotberg 1994; Eckmann & Lomivorotov 2003; Suzuki & Eckman 2003; Barak & Yeshayahu 2005; Li *et al.* 2021), microcirculation and oxygen transport in blood vessels (e.g. Berg *et al.* 2020; Vadapalli, Goldman & Popel 2002) and targeted microbubbles for drug delivery (e.g. Bull 2005). In the context of microfluidics, small-scale reactors, cell cultures and cooling devices rely on an efficient control of transport processes in microchannels, (e.g. Ajaev & Homsy 2006; Lynn 2016; Khodaparast *et al.* 2017). All the aforementioned applications involve the motion of elongated bubbles (also known as Taylor bubbles) through capillaries where surface mass-transfer mechanisms take place between the surrounding liquid, the solid and the bubble interface. Exchanges of mass could be driven either by chemical reactions or surface phenomena, such as evaporation or dissolution. Thus, studying how mass transfer is enhanced or retarded due to the presence of a confined bubble is highly important for a correct interpretation of practical problems.

So far, many researchers have focused primarily on understanding the hydrodynamics of Taylor bubbles in capillary tubes in regimes where viscous forces and surface tension dominate over buoyancy and inertia. The seminal work of Bretherton (1961) revealed that bubble characteristics (i.e. the film thickness, the bubble speed) can be expressed as a function of the capillary number and that the film profile can be described with a similarity solution typical of Landau–Levich–Derjaguin–Bretherton problems (see de Gennes, Brochard-Wyart & Quéré 2003; Stone 2010). The theory is supported by several experimental measurements (Fairbrother & Stubbs 1935; Taylor 1961; Schwartz, Princen & Kiss 1986; Aussillous & Quéré 2000) and, in the last decades, it has been extended to include the effect of viscous forces and weak inertia (Cox 1962; Reinelt & Saffman 1985; Aussillous & Quéré 2000; Heil 2001; de Ryck 2002; Khodaparast *et al.* 2015; Magnini *et al.* 2017), unsteady flow, (Yu *et al.* 2018), buoyancy, (Leung *et al.* 2012; Atasi *et al.* 2017; Lamstaes & Eggers 2017), bubble viscosity and non-Newtonian effects (Chen 1986; Hodges, Jensen & Rallinson 2004; Balestra, Zhu & Gallaire 2018; Shukla *et al.* 2019; Picchi *et al.* 2021).

However, the case where a passive scalar (i.e. a solute) is transported in the liquid surrounding the Taylor bubble is still an object of research. Motivated by the discrepancies between experiments and Bretherton's theory, Schwartz *et al.* (1986), Hirasaki & Lawson (1985) and Ginley & Radke (1988) accounted for the effect of variation in the surface tension due to the presence of surface-active contaminants (i.e. the Marangoni effect) in the uniform film region. Ratulowski & Chang (1990) have shown that the Marangoni effect can explain the increased film thickness of the experiments; more recent studies (Park 1992; Stebe & Barthés-Biesel 1995; Olgac & Muradoglu 2013; Yu, Khodaparast & Stone 2017) confirm the importance of accessing the transport problem in the surroundings of the bubble to properly describe solute driven mechanisms.

Unfortunately, the problem of solute transport by advection and diffusion in confined geometries is a long standing issue. The seminal works of Taylor (1953) and Aris (1956) showed that the flow of a passive scalar in a circular pipe enhances axial diffusion. Although the Aris–Taylor dispersion theory was later extended to cases where the solute can be also absorbed from the solid walls (e.g. Gupta, Gupta & Taylor 1972; Sankarasubramanian, Gill & Benjamin 1973; Ng 2006; Mikelić, Devigne & van Duijn 2006), to the best of our knowledge, a comprehensive approach to generalise the transport problem in the presence of moving Taylor bubbles is still missing in the literature.

Existing studies on the topic are primarily numerical and experimental. Shim *et al.* (2014), Michelin, Guérin & Lauga (2018) and Rivero-Rodriguez & Scheid (2019) studied mass transfer around a series of spherical bubbles. Other works focus on quantifying mass-transfer fluxes around gaseous Taylor bubbles in horizontal (e.g. Yue *et al.* 2009; Shao, Gavriilidis & Angeli 2010; Sobieszuk *et al.* 2011; Cubaud, Sauzade & Sun 2012; Ganapathy, Al-Hajri & Ohadi 2013; Ganapathy *et al.* 2014; Jia & Zhang 2016; Svetlov & Abiev 2016; Zhu *et al.* 2017; Silva, Campos & Araújo 2019; Zhou *et al.* 2020) and vertical (e.g. Hayashi *et al.* 2014; Kastens *et al.* 2015; Hori *et al.* 2020) microchannels. Despite the amount of data available, in most of the cases experiments are analysed only in terms of empirical correlations. More sophisticated theories for modelling transport processes in complex geometries based on averaging and homogenisation techniques are available in the field of flow in porous materials (e.g. Brenner & Stewartson 1980; Rubinstein & Mauri 1986; Mauri 1991; Battiato & Tartakovsky 2011; Parmigiani *et al.* 2011; Picchi & Battiato 2018), but an attempt to adapt those theories to the case of a Taylor bubble has not been proposed yet.

To fill this gap, the goal of this paper is to study the transport problem around a moving Taylor bubble in the presence of surface mass transfer and to clarify the competition between diffusion, advection and superficial mass transfer in the different regions of the bubble. We account for the transport of a solute in the bulk of the fluid surrounding the Taylor bubble and surface mass-transfer effects at the wall and at the bubble–fluid interface. Our goal is to derive a theoretical framework to describe in a rigorous way the transport problem, including transient effects. The model generalises the Aris–Taylor dispersion theory to the case of a Taylor bubble and allows for the identification of the dominant transport regime in the front and rear menisci and in the uniform film region (i.e. the bubble centre).

With this aim, starting from the transport equations (§ 2.2), we derive an upscaled model for the average concentration by means of two-scale asymptotic expansions (§ 2.3). Specifically, we derive analytical expressions for the effective velocity, effective diffusion and effective mass-transfer coefficient in an advection–diffusion–mass-transfer equation that describes the evolution of the averaged concentration as a function of space and time (§ 2.4). Our approach (the full derivation is presented in Appendix B) allows us to determine the theoretical bounds of validity of the model, expressed in terms of the governing dimensionless numbers. The analysis is complemented by a classification of the dominant transport regimes depending on the magnitude of the Pèclet and Sherwood numbers of the problem (§ 2.5). Then, we solve numerically the advection–diffusion–mass-transfer equation coupled with the bubble profile (Bretherton 1961) to study the transport problem in the bubble front and the bubble rear (§§ 3.1 and 3.2). In a separate section (§ 3.3), we present the analytical solution of the transport problem in the uniform film region. The results shed light on the mechanisms that control the transport of a passive scalar around a Taylor bubble in the presence of superficial mass transfer.

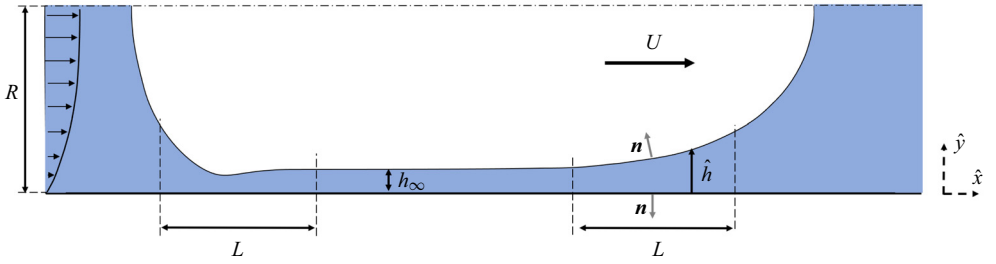

Figure 1. Sketch of the confined bubble that moves at speed U within a channel of half-width R. The film regions of length L of the front and rear menisci are depicted. The Taylor bubble is sufficiently long so that a region of uniform film thickness h_∞ exists.

2. Theoretical derivation

2.1. *Viscous flow in the film*

We consider a Taylor bubble confined in an horizontal planar channel that advances through an incompressible Newtonian fluid at a steady velocity U, as sketched in figure 1. The motion is driven by a Poiseuille flow with a constant average velocity far ahead of the bubble, see figure 1. The bubble is sufficiently long so that a region with uniform film thickness h_∞ exists and $h_\infty/R \ll 1$. In the limit of small capillary number, the slope of the interface in the film is small $\mathrm{d}\hat{h}/\mathrm{d}\hat{x} \ll 1$ and the dynamics of $\hat{h}(\hat{x}, \hat{t})$ is described by the lubrication equation (Eggers & Fontelos 2015)

$$\frac{\partial \hat{h}}{\partial \hat{t}} + \frac{\sigma}{3\mu}\frac{\partial}{\partial \hat{x}}\left(\hat{h}^3 \frac{\partial^3 \hat{h}}{\partial \hat{x}^3}\right) = 0, \tag{2.1}$$

where μ and σ are the liquid viscosity and surface tension, respectively. Equation (2.1) describes the motion in the film region in response to the gradient of the capillary pressure $\hat{p} = -\sigma\, \mathrm{d}^2\hat{h}/\mathrm{d}\hat{x}^2$. In a moving reference frame attached to the bubble $\hat{h}(\hat{x}, \hat{t}) = \hat{h}(\hat{x} - U\hat{t})$, the integration of (2.1) yields to the Landau–Levich–Derjaguin–Bretherton similarity equation (see de Gennes *et al.* 2003; Stone 2010)

$$\frac{\mathrm{d}^3\eta}{\mathrm{d}x^3} = \frac{\eta - 1}{\eta^3}, \tag{2.2}$$

where

$$x = \frac{\hat{x}}{h_\infty (3Ca)^{-1/3}}, \quad \eta = \frac{\hat{h}}{h_\infty}, \quad Ca = \frac{\mu U}{\sigma}. \tag{2.3a–c}$$

This is the film equation derived by Bretherton (1961) that describes the transition region between the film and the caps at either end. At the bubble front, (2.2) can be integrated numerically starting from the uniform film, which corresponds to the boundary condition $\eta(-\infty) = 1$, towards $x \to \infty$ where the solution matches to a spherical cap of radius R. In the vicinity of the uniform film, the solution has an exponential behaviour, while, for $\eta \gg 1$ a parabolic region with constant dimensionless curvature $\mathrm{d}^2\eta/\mathrm{d}x^2$ is established. To get the profile at the bubble rear, (2.2) is integrated in the opposite direction towards $x \to -\infty$ starting from the uniform film region. Imposing that the rear curvature far from the uniform has the same curvature of the front, the typical oscillating profile at the back is obtained. All the details for the computation of the bubble profile are described in Bretherton (1961).

2.2. Governing equations for transport

We consider the transport of a scalar of concentration $c(\hat{x}, \hat{y}, \hat{t})$ within the film region of a confined Taylor bubble. The scalar is advected by the velocity field and diffuses with a constant diffusion coefficient D. In a reference frame attached to the bubble, the governing equation for the concentration reads

$$\frac{\partial \hat{c}}{\partial \hat{t}} + \left[\hat{u} - U\right] \frac{\partial \hat{c}}{\partial \hat{x}} + \hat{v} \frac{\partial \hat{c}}{\partial \hat{y}} = D \frac{\partial^2 \hat{c}}{\partial \hat{x}^2} + D \frac{\partial^2 \hat{c}}{\partial \hat{y}^2}, \quad \hat{y} \in [0, \hat{h}], \tag{2.4}$$

where $\hat{u}$ and $\hat{v}$ are the local velocity in the x and y directions, respectively. According to Bretherton (1961), the flow in the film region is expressed using a lubrication approximation with $\hat{u}(\hat{x}, \hat{y})$ and $\hat{v}(\hat{x}, \hat{y})$ given in (A1) and (A3), respectively. We assume that at the bottom wall, $\hat{y} = 0$, and the bubble–fluid interface, $\hat{y} = \hat{h}$, the scalar is transferred with first-order mass-transfer coefficients k_w and k_i, respectively, as described by the following boundary conditions:

$$-D \nabla \hat{c}\big|_0 \cdot \boldsymbol{n} = k_w \hat{c} \quad \text{at } \hat{y} = 0, \tag{2.5}$$

$$-D \nabla \hat{c}\big|_{\hat{h}} \cdot \boldsymbol{n} = k_i \hat{c} \quad \text{at } \hat{y} = \hat{h}, \tag{2.6}$$

where $\boldsymbol{n}$ is the unit vector perpendicular to the boundary pointing out of the fluid domain, see figure 1. At the wall, the normal unit vector is $\boldsymbol{n} = (0, -1)$ while at the bubble–fluid interface the unit vector depends on the meniscus profile as

$$\boldsymbol{n} = \left(-\frac{\partial \hat{h}/\partial \hat{x}}{\sqrt{1 + (\partial \hat{h}/\partial \hat{x})^2}}, \frac{1}{\sqrt{1 + (\partial \hat{h}/\partial \hat{x})^2}} \right)^{\mathrm{T}}. \tag{2.7}$$

Before recasting the transport equation in terms of dimensionless variables, it is worth identifying the characteristic scales of the problem. The two relevant length scales in the $\hat{x}$ and $\hat{y}$ directions are the characteristic length of the film region, $L = h_\infty (3Ca)^{-1/3}$ from Bretherton (1961), and the uniform film thickness h_∞. Based on these, we define the following scale parameter:

$$\varepsilon = \frac{h_\infty}{L} = (3Ca)^{1/3} \ll 1. \tag{2.8}$$

The determination of the relevant time scale is not unique (e.g. Mauri 1991; Auriault & Adler 1995; Mikelić *et al.* 2006; Battiato & Tartakovsky 2011; Bourbatache, Millet & Moyne 2020). Assuming that the characteristic scale for the velocity is the bubble speed U, we can define the axial advective time $\tau_a = L/U$. Molecular diffusion introduces two additional time scales, the axial, $\tau_L = L^2/D$, and the transverse, $\tau_h = h_\infty^2/D$, diffusion times. Since we are primarily interested in transport dynamics in a time frame much larger than the transverse diffusion time and close to the advection time, we choose τ_a as the reference scale for the time variable.

The presence of superficial mass transfer introduces additional time scales in the axial, $\tau_{Lw} = L/k_w$ and $\tau_{Li} = L/k_i$, and the transverse, $\tau_{hw} = h_\infty/k_w$ and $\tau_{hi} = h_\infty/k_i$, directions. As discussed later, we focus on the most general case when the transversal mass transfer balances with axial advection.

We make (2.4) dimensionless with

$$x = \frac{\hat{x}}{L}, \quad y = \frac{\hat{y}}{h_\infty}, \quad t = \frac{\hat{t}}{\tau_a}, \quad u = \frac{\hat{u}}{U}, \quad v = \frac{\hat{v}}{\varepsilon U}, \quad c = \frac{\hat{c}}{c_{ref}}, \tag{2.9a–f}$$

where c_{ref} is a reference value for the concentration. This procedure yields

$$\frac{\partial c}{\partial t} + [u-1]\frac{\partial c}{\partial x} + v\frac{\partial c}{\partial y} = \frac{1}{Pe}\frac{\partial^2 c}{\partial x^2} + \frac{1}{Pe\varepsilon^2}\frac{\partial^2 c}{\partial y^2}, \quad y \in [0, \eta]. \tag{2.10}$$

where $u(x, y)$ and $v(x, y)$ are given in (A7) and (A8), respectively. The Pèclet number Pe is defined as

$$Pe = \frac{LU}{D} = \frac{\tau_L}{\tau_a}, \tag{2.11}$$

and can be interpreted as the ratio between advection and diffusion in the axial direction or, alternatively, between the diffusion and the advection time scales. When the Pèclet number is small, $Pe \ll 1$, the problem is diffusion dominated; when $Pe = O(1)$ diffusion and advection play similar roles; for $Pe \gg 1$ the problem is advection dominated. The dimensionless boundary conditions at the wall and at the bubble–fluid interface read

$$\frac{\partial c}{\partial y} = \varepsilon^2 Sh_w\, c, \quad \text{at } y = 0, \tag{2.12}$$

$$\frac{\varepsilon^2 \partial\eta/\partial x}{\sqrt{1+\varepsilon^2(\partial\eta/\partial x)^2}}\frac{\partial c}{\partial x} - \frac{1}{\sqrt{1+\varepsilon^2(\partial\eta/\partial x)^2}}\frac{\partial c}{\partial y} = \varepsilon^2 Sh_i\, c, \quad \text{at } y = \eta, \tag{2.13}$$

where

$$Sh_w = \frac{L^2 k_w}{h_\infty D} = \frac{\tau_L}{\tau_{hw}} \quad Sh_i = \frac{L^2 k_i}{h_\infty D} = \frac{\tau_L}{\tau_{hi}}, \tag{2.14a,b}$$

are the Sherwood numbers for the wall and interfacial mass-transfer mechanisms. Both Sherwood numbers are the ratio between transversal mass transfer and axial diffusion: for finite Sh, superficial mass transfer competes with advection and diffusion; for $Sh \ll 1$ superficial mass transfer becomes negligible. Under the assumption that the lubrication approximation for the film, equation (2.2) holds, i.e. $\varepsilon \ll 1$, (2.13) simplifies to

$$-\frac{\partial c}{\partial y} = \varepsilon^2 Sh_i c, \quad \text{at } y = \eta. \tag{2.15}$$

In other words, the slope of the bubble–fluid interface is sufficiently small, $\mathrm{d}\hat{h}/\mathrm{d}\hat{x} \ll 1$, that the unit vector (2.7) almost aligns with the y axis in figure 1, i.e. $\boldsymbol{n} = (0, 1)$ at the bubble–fluid interface.

2.3. *Two-scale asymptotic expansion of the transport equation*

The goal of this work is to obtain a one-dimensional approximation of the transport equation in the film region. We seek to account for advection, diffusion and superficial mass-transfer mechanisms through an effective velocity, effective diffusion and effective mass-transfer coefficient in an advection–diffusion–mass-transfer equation. To do so, we

proceed using a two-scale asymptotic expansion (Hornung 1997; Bensoussan, Lions & Papanicolaou 2011; Boutin, Auriault & Geindreau 2010):

(i) The starting point is the local description of the transport problem in dimensionless form, see (2.10), (2.12) and (2.15), where we define the scale parameter $\varepsilon = (3Ca)^{1/3} \ll 1$, see (2.8). Specifically, the proposed asymptotic expansion holds in the limit of small capillary numbers, $Ca \ll 1$, as constrained by Bretherton's theory.

(ii) The governing dimensionless numbers are evaluated with respect to the scale parameter – or the capillary number – as

$$Pe = \varepsilon^{-\alpha}, \quad Sh_w = \varepsilon^{\beta}, \quad Sh_i = \varepsilon^{\gamma}, \tag{2.16a–c}$$

where the exponents α, β and γ characterise the system behaviour.

(iii) The concentration field $c(x, y, t)$ is expanded in (2.10), (2.12) and (2.15) as a perturbation series in the scale parameter as follows:

$$c = c_0(x, y, t) + \varepsilon c_1(x, y, t) + \varepsilon^2 c_2(x, y, t) + \dots. \tag{2.17}$$

(iv) Then, after collecting the terms with the same order, the successive boundary-value problems are solved to obtain the effective description of the transport problem in terms of the film-averaged concentration

$$\langle c \rangle = \frac{1}{\eta} \int_0^{\eta} c(x, y, t)\, \mathrm{d}y, \tag{2.18}$$

plus higher-order corrections. Specifically, the zeroth-order term in (2.17) is independent on y and, therefore, $c_0(x, t) = \langle c \rangle(x, t)$.

(v) The last step is checking if the aforementioned procedure yields the desired result (the existence of an effective description in terms of the average concentration) or conditions where the coupling between scales prevents the existence of an equivalent effective description. The parameter space where this result holds is rigorously determined and the applicability conditions of the model can be mapped in terms of Pe, Sh_w and Sh_i.

The full derivation is provided in Appendix B, distinguishing between three main transport regimes: advection dominated, competition between advection and diffusion and diffusion dominated. The final result of this procedure is given in the next section.

2.4. *The one-dimensional advection–diffusion–mass-transfer equation*

The advection–diffusion–mass-transfer equation describing the transport of the averaged concentration in the film region of a Taylor bubble is given by

$$\frac{\partial \langle c \rangle}{\partial t} + (u^\star - 1)\, \frac{\partial \langle c \rangle}{\partial x} + \frac{Sh^\star}{Pe} \langle c \rangle = \frac{D^\star}{Pe} \frac{\partial^2 \langle c \rangle}{\partial x^2}, \tag{2.19}$$

where $u^\star$, $Sh^\star$ and $D^\star$ are the effective velocity, the effective Sherwood number and the effective diffusion coefficient, respectively, defined as

$$u^\star = \frac{\eta - 1}{3\eta} - \varepsilon^2 Pe\, \frac{(73\eta - 8)(\eta - 1)}{3780\eta} \frac{\mathrm{d}\eta}{\mathrm{d}x} - \varepsilon^2 Sh_i \frac{14\eta(\eta - 1) + (73\eta + 47)\, \mathrm{d}\eta/\mathrm{d}x}{360\eta} + \varepsilon^2 Sh_w \frac{16\eta(\eta - 1) + (47\eta + 13)\, \mathrm{d}\eta/\mathrm{d}x}{360\eta}, \tag{2.20}$$

$$Sh^\star = \frac{Sh_w + Sh_i}{\eta} + \frac{\varepsilon^2}{3}\left(Sh_w\, Sh_i - Sh_w^2 - Sh_i^2\right) - \varepsilon^2 Pe \frac{Sh_i(7\eta - 18) + Sh_w(7 - 3\eta)}{120\eta}\frac{\mathrm{d}\eta}{\mathrm{d}x}, \tag{2.21}$$

$$D^\star = 1 + \varepsilon^2 Pe^2 \frac{2(\eta - 1)^2}{945}. \tag{2.22}$$

The effective coefficients of (2.19) incorporate the impact of shear flow in the film and the changes in the bubble shape. Specifically, the shear flow spreads the concentration distribution in the axial direction, enhancing the axial diffusion coefficient $D^\star$ at sufficiently large Péclet numbers. At the same time, changes in the curvature of the bubble along the axial direction affect the pressure gradient (that drives the flow), and both $u^\star$ and $Sh^\star$.

The effective advection accounts for the contribution of three mechanisms: the velocity in the axial direction (the first term in (2.20)), the coupled effect of bubble shape and the velocity field in both the axial and transverse directions (the second term in (2.20)), superficial mass-transfer mechanisms at the boundaries (the last two terms in (2.20)).

The presence of surface mass transfer translates to a source term in (2.19) whose intensity is controlled by the effective Sherwood number. The source term acts to diminish the averaged concentration ($Sh^\star$ is always positive) as a consequence of how the boundary conditions (2.12) and (2.15) are formulated, i.e. assuming outflow fluxes at the boundaries. By inspection of (2.21), we can see that the effective mass transfer accounts for the contribution of the bubble shape (the first term in (2.21)) and the coupled effect of local advection and changes in the bubble shape (the last term in (2.21)).

The evolution of the effective coefficients in different regions of the bubble and their physical origins will be discussed § 3. In Appendix C, we will show that only the leading term in (2.20) and (2.21) contributes to the overall $u^\star$ and $Sh^\star$ in both the front and the rear menisci.

Concerning the applicability of the effective equation, (2.19) holds only if the following conditions are met:

(i) $\varepsilon \ll 1$;
(ii) $Pe \ll O(\varepsilon^{-2})$;
(iii) $Sh_w \ll O(\varepsilon^{-2})$ and $Sh_i \ll O(\varepsilon^{-2})$;
(iv) $Sh_i/Pe \ll O(\varepsilon^{-1})$ and $Sh_w/Pe \ll O(\varepsilon^{-1})$.

Condition (i) ensures the $x - y$ scale separation holds, i.e. the film region is much longer compared with thickness of the uniform film. Conditions (ii) and (iii) provide the upper bounds to the Pèclet and the Sherwood numbers, identifying the parameter space for which it is possible to derive an effective transport equation for the averaged concentration. Condition (iv) ensures that mass-transfer mechanisms do not prevail over advection.

2.5. *Identification of transport regimes*

In this section we clarify the competition between advection, diffusion and mass transfer in the film surrounding a Taylor bubble, defining different transport regimes for (2.19). To do so, we summarise the regimes in a phase diagram based on the magnitude of the Pèclet and Sherwood numbers, see figure 2. The coloured regions of figure 2 refer to

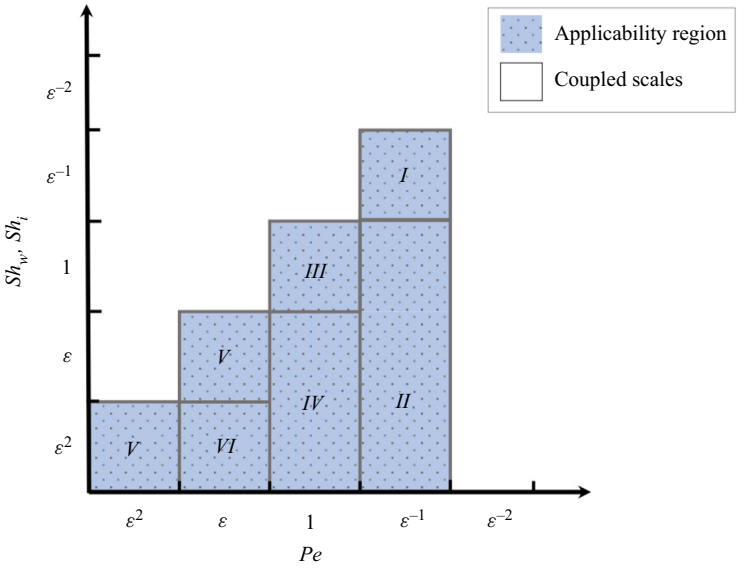

Figure 2. Phase diagrams of transport regimes in the Pe–Sh_w or Pe–Sh_i planes. Coloured areas correspond to regimes where the effective transport equation for the film-averaged concentration can be formally written by means of two-scale expansions. We identify the following transport regimes: I, effective advection, effective diffusion and effective mass transfer; II, effective advection and effective diffusion; III, effective advection, molecular diffusion and effective mass transfer; IV, effective advection and molecular diffusion; V, molecular diffusion and effective mass transfer; VI, molecular diffusion only.

physical conditions where the transport equation for the film-averaged concentration can be formally written by means of two-scale expansions. Outside the coloured regions the scales are coupled. In the phase diagram, the roles of the Sherwood number at the wall, Sh_w, and the interface, Sh_i, are equivalent since they appear with the same functional dependence in (2.20) and (2.21).

When the Pèclet number is large ($Pe = O(\varepsilon^{-1})$) and at least one of the two Sherwood numbers is of the order of $O(\varepsilon^{-1})$, the transport is driven by the competition between effective advection, effective diffusion and effective mass transfer as

$$\text{Regime I:} \quad \frac{\partial \langle c\rangle}{\partial t} + (u^\star - 1)\,\frac{\partial \langle c\rangle}{\partial x} + \varepsilon\, Sh_I^\star \langle c\rangle = \varepsilon\, D_I^\star \frac{\partial^2 \langle c\rangle}{\partial x^2}, \tag{2.23}$$

$$\text{with} \quad D_I^\star \sim 1 + \frac{2(\eta-1)^2}{945}, \quad Sh_I^\star \sim \frac{1}{\varepsilon\eta}, \quad u^\star \sim \frac{\eta-1}{3\eta}, \tag{2.24}$$

where we have used the approximations given in Appendix C. Near the uniform film where $\eta = O(1)$, shear and shape induced diffusion is negligible since the fluid is nearly at rest. Therefore, the effective diffusion coefficient reduces to molecular diffusion, $D_I^\star \approx 1$. Far from the uniform film, instead, shear-flow and shape induced diffusion plays a role augmenting $D_I^\star$. The effective mass-transfer coefficient $Sh_I^\star$ plays a role only in the proximity of the uniform film where the surface available to mass transfer is high compared with the amount of fluid. If $\eta \gg 1$, $Sh_I^\star$ becomes negligible. For smaller Sherwood numbers, $Sh_i \ll O(\varepsilon^{-1})$ and $Sh_w \ll O(\varepsilon^{-1})$, the source term in (2.23) can be dropped; we refer to this case as regime II.

When the Pèclet number is finite ($Pe = O(1)$) and at least one of the Sherwood numbers is of the order of $O(1)$, effective advection competes with effective mass transfer and molecular diffusion leading to

$$\text{Regime III:} \quad \frac{\partial \langle c \rangle}{\partial t} + (u^\star - 1)\frac{\partial \langle c \rangle}{\partial x} + Sh^\star_{III}\langle c \rangle = D^\star_{III}\frac{\partial^2 \langle c \rangle}{\partial x^2}, \tag{2.25}$$

$$\text{with} \quad D^\star_{III} \approx 1, \qquad Sh^\star_{III} \sim \frac{1}{\eta}. \tag{2.26}$$

In this regime, shear and shape induced diffusion becomes negligible. In case the Sherwood numbers are smaller, the mass-transfer term in (2.25) can be dropped (regime IV).

When the Pèclet number is small ($Pe = O(\varepsilon)$) and at least one of the Sherwood numbers is of the order of $O(\varepsilon)$, transport is purely driven by molecular diffusion and advection plays a negligible role. Specifically,

$$\text{Regime V:} \quad Pe\frac{\partial \langle c \rangle}{\partial t} + Sh^\star_V\langle c \rangle = D^\star_V\frac{\partial^2 \langle c \rangle}{\partial x^2}, \quad \text{with } D^\star_V = 1, \tag{2.27}$$

where the mass-transfer term can be dropped when Sh_w and Sh_i assumes smaller values (regime VI), see figure 2.

2.6. *Numerical solution*

The general solution of (2.19) can be found numerically for the front and rear menisci if the film profile and the boundary and initial conditions for the averaged concentration are provided.

The film profile, $\eta(x)$, is obtained solving (2.2) for the rear and the front menisci separately, as discussed in § 2.1, using the differential equation solver *ode45* of Matlab. The code used in this work for this purpose has been developed in a previous publication (Picchi *et al.* 2021), where all the details concerning the boundary conditions are discussed.

The concentration field $\langle c \rangle(x, t)$ is obtained solving (2.19) using the solver *pdepe* of Matlab. A different set of initial and boundary conditions is considered and will be discussed in the following sections. The front and the rear menisci are treated separately and, since the effective coefficients depend on the local film thickness $\eta(x)$, we developed a Matlab function that provides the film thickness at a specific location to evaluate the coefficients of (2.19).

3. Results and discussion

3.1. *The concentration field in the front meniscus*

In this section, we investigate how the solute is transported within the film region in the bubble front. Figure 3(*a*) shows the typical profile of the front meniscus (black line): close to the uniform film region the interface grows slowly (exponential region with $\eta \sim \exp(x)$) while, for $\eta \gg 1$, the profile follows a parabolic trend ($\eta \sim 0.321x^2$ as in Bretherton 1961). The following analysis assumes that the scale parameter is sufficiently small so that the concentration field can be expanded as in (2.17), i.e. $\varepsilon = 0.01$.

Diffusion is controlled by the effective diffusion coefficient $D^\star$ defined in (2.22). In the uniform film region, $\eta = 1$, the fluid is at rest and only molecular diffusion plays a role,

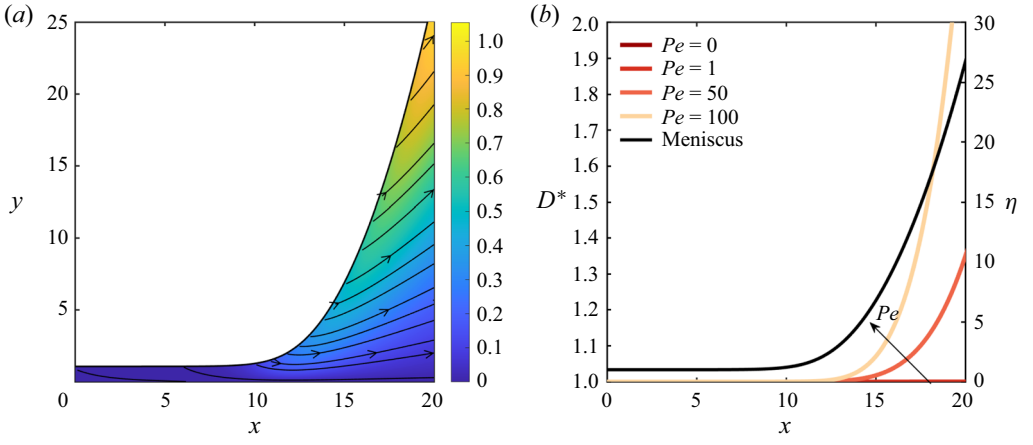

Figure 3. (*a*) Contours of the magnitude of the velocity, $\sqrt{u(x,y)^2 + v(x,y)^2}$ and flow streamlines with respect to a fixed reference frame in the bubble front; (*b*) effect of Pèclet number on the effective diffusion coefficient, $D^\star$, in the front meniscus; right, profile of the front meniscus; $\varepsilon = 0.01$.

$D^\star = 1$. In the front meniscus, instead, the shear flow tends to spread the scalar along the axial direction (see the streamlines in figure 3*a*) enhancing the effective diffusion at sufficiently large Péclet numbers. This effect is the combination of the local axial velocity field and changes in bubble shape, as shown in figure 3(*b*). For the sake of physical interpretation, we can recast (2.22) in terms of the Pèclet number of the film, Pe_f,

$$D^\star = 1 + Pe_f^2 \frac{2}{945} \quad \text{where } Pe_f = \frac{U(\hat{h} - h_\infty)}{D}, \tag{3.1}$$

recovering the same scaling law of the Aris–Taylor dispersion coefficient. In other words, the effective diffusion coefficient follows a Pèclet square behaviour.

The effective velocity given in (2.20) is negligible only in the uniform film region. As the magnitude of the velocity becomes relevant, see figure 3(*a*), the averaged concentration experiences additional advection, as plotted in figure 4. The major contribution comes from the axial velocity which follows a $(\eta - 1)/3\eta$ behaviour and reaches the limiting value of $u^\star \to 1/3$. The effective velocity slightly diminishes as an effect of Pe and Sh_i when η is high; the evolution of $u^\star$ with respect to Sh_w is not shown for the sake of brevity. Interestingly, the contribution of the wall and interfacial Sherwood numbers, Sh_w and Sh_i, appear with opposite sign in (2.20). This can be explained with differences in the local velocity between the channel wall (where the velocity is zero due to the no-slip condition) and the bubble–fluid interface (where the velocity is non-zero according to the free-surface boundary condition).

The effective Sherwood number, (2.21), is maximum in the uniform film region. There, since the fluid is at rest, the solute cannot escape the film and, therefore, it is rapidly consumed from the boundaries. Outside of the uniform film region, $Sh^\star$ decays as η^{-1} since the non-zero velocity causes the scalar to escape the surface, see figure 4(*c*). Note that the second and the third terms in (2.21) make only small contributions to the overall $Sh^\star$, meaning that the effective mass transfer is mostly driven by the proximity to the boundaries (i.e. the bubble shape) via the variable η.

In order to identify which mechanism dominates, we construct the following representative test case. We solve (2.19) imposing a concentration front $\langle c \rangle(x_0, t) = 1$ at $x \geqslant x_0$ and initialising $\langle c \rangle(x, 0) = 0$ in the entire domain. Since the location of the

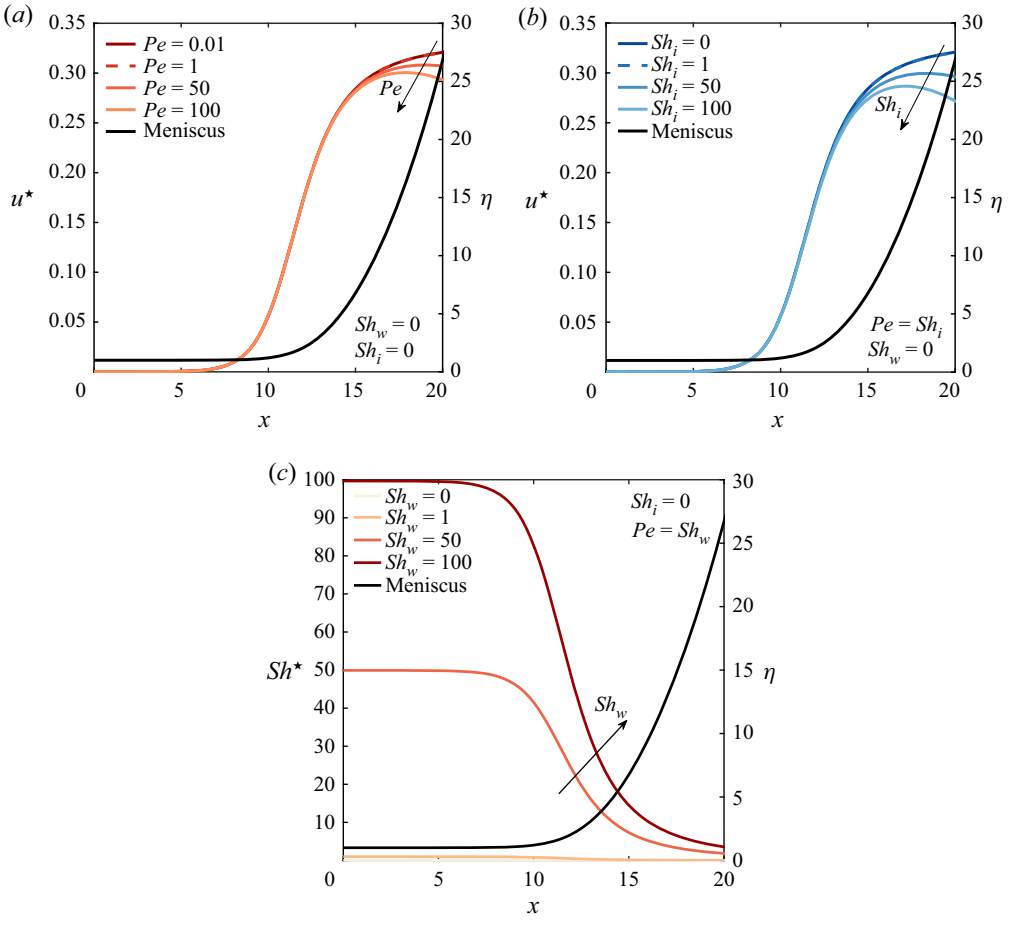

Figure 4. Effective velocity in the front meniscus. (*a*) Left, effect of *Pe*; right, profile of the front meniscus. (*b*) Left, effect of mass transfer at the bubble–fluid interface; right, profile of the front meniscus. (*c*) Left, effect of the Sherwood number at the wall; right, profile of the front meniscus. The evolution of Sh_i is not shown since there is no discernible difference from $Sh^\star$. In all cases $\varepsilon = 0.01$.

concentration front is purely arbitrary, we chose to place it at $x_0 = 20$. This choice ensures that the concentration front is sufficiently far from the transition between the exponential region (where $\eta \approx 1$) and the parabolic region. In this way, we inject the solute into a region where the dimensionless curvature is constant. This set-up mimics the case where the bubble advances through a 'dirty' (i.e. sharp discontinuity in the concentration field) channel. Specifically, we show the transient dynamics of the most general case, regime I defined in § 2.5, and the transitions to regimes II, III and IV.

Figure 5 shows the time evolution of the average of the concentration along the front meniscus for a regime where advection dominates over diffusion and superficial mass transfer balances with advection. Specifically, we refer to a case where $Pe = 100$, $Sh_w = 100$ and $Sh_i = 0$ (regime I). At $t = 1$, see figure 5(*a*), the concentration front is sharp, while at later times, the front gets more and more diffuse. Interestingly, as the front gets closer to the uniform film region, the concentration rapidly decreases since the effective Sherwood number $Sh^\star$ in (2.19) becomes dominant, see figure 4(*c*); the movie of this case is available as supplementary Movie 1 available at https://doi.org/10.1017/jfm.2022.829.

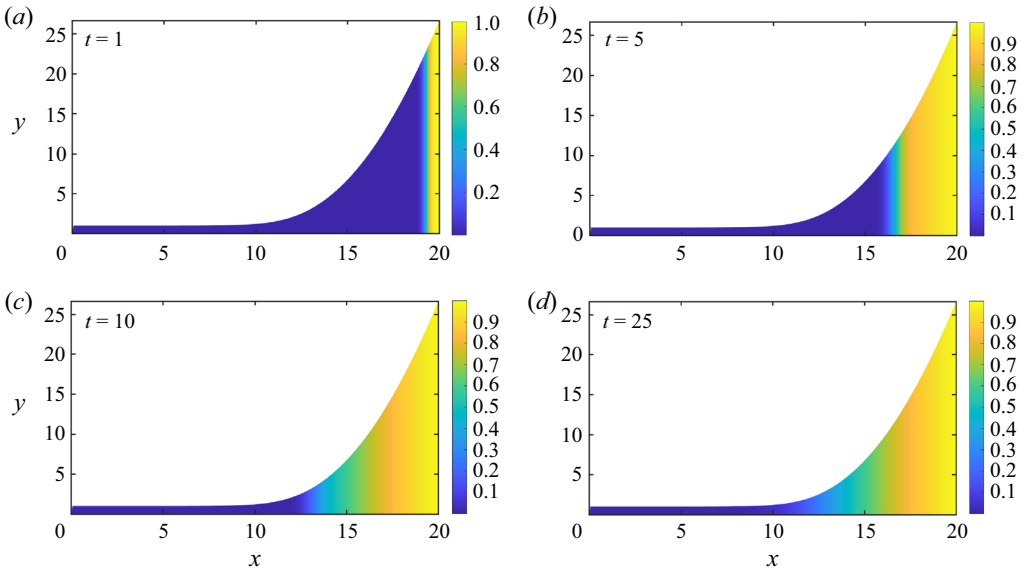

Figure 5. Time evolution of the average of the concentration, $\langle c\rangle(x,t)$, in the bubble front for $Pe = 100$, $Sh_w = 100$, $Sh_i = 0$ and $\varepsilon = 0.01$. Note that the quantity plotted is a one-dimensional approximation of a two-dimensional field. See online supplementary Movie 1 for a simulation of this case.

To get a more quantitative picture, we present the breakthrough curves in figure 6(*e*): the solute is entirely consumed even before reaching the uniform region. In this regime, even though the bubble advances through a 'dirty' channel, we expect the uniform film region to be 'clean' from the solute at later times.

When the surface mass transfer is reduced to $Sh_w/Pe = 0.1$, the decay of the passive scalar in the film region is less intense and, at later times, the front propagates inside the uniform film region, see figure 6(*c*). In case $Sh_w = 0$ (regime II), the front propagates almost rigidly except for the effect of weak diffusion, see figure 6(*a*).

When diffusion and advection compete for $Pe = 1$ (regimes III–IV), the breakthrough curves assume a different shape, see figure 6(*b*,*d*,*f*). At early times, the front is rapidly diffused independently of the magnitude of the Sherwood number and an increase of Sh_w results in a more intense decay in the film region. Also for this regime, when $Pe \sim Sh_w$ the solute is consumed even before reaching the uniform film. Note that we only show the impact of the wall mass-transfer mechanism, but analogous results are obtained for mass transfer at the bubble–fluid interface imposing $Sh_i \neq 0$.

The effect of the Pèclet and Sherwood numbers is summarised in figure 7, where we show the breakthrough curves at the steady state, $\langle c\rangle(x, t \to \infty)$. Each steady state curve represents the envelope of the transient behaviour described in figure 6. As expected, when $Sh_w = 0$, the mass-transfer mechanism does not play any role and, therefore, the steady state is the trivial solution $\langle c\rangle = 1$. As Sh_w increases, instead, the solute is quickly consumed: the location where $\langle c\rangle \approx 0$ shifts closer to the concentration source, see figure 7(*a*). The Pèclet number affects the steady state behaviour by shifting the breakthrough curve in the direction of the uniform film (i.e. enhancing the effect of advection), see figure 7(*b*).

Another aspect of interest for applications is the formation of hot spots in the concentration field, which may determine localised mass-transfer fluxes. To see this, we

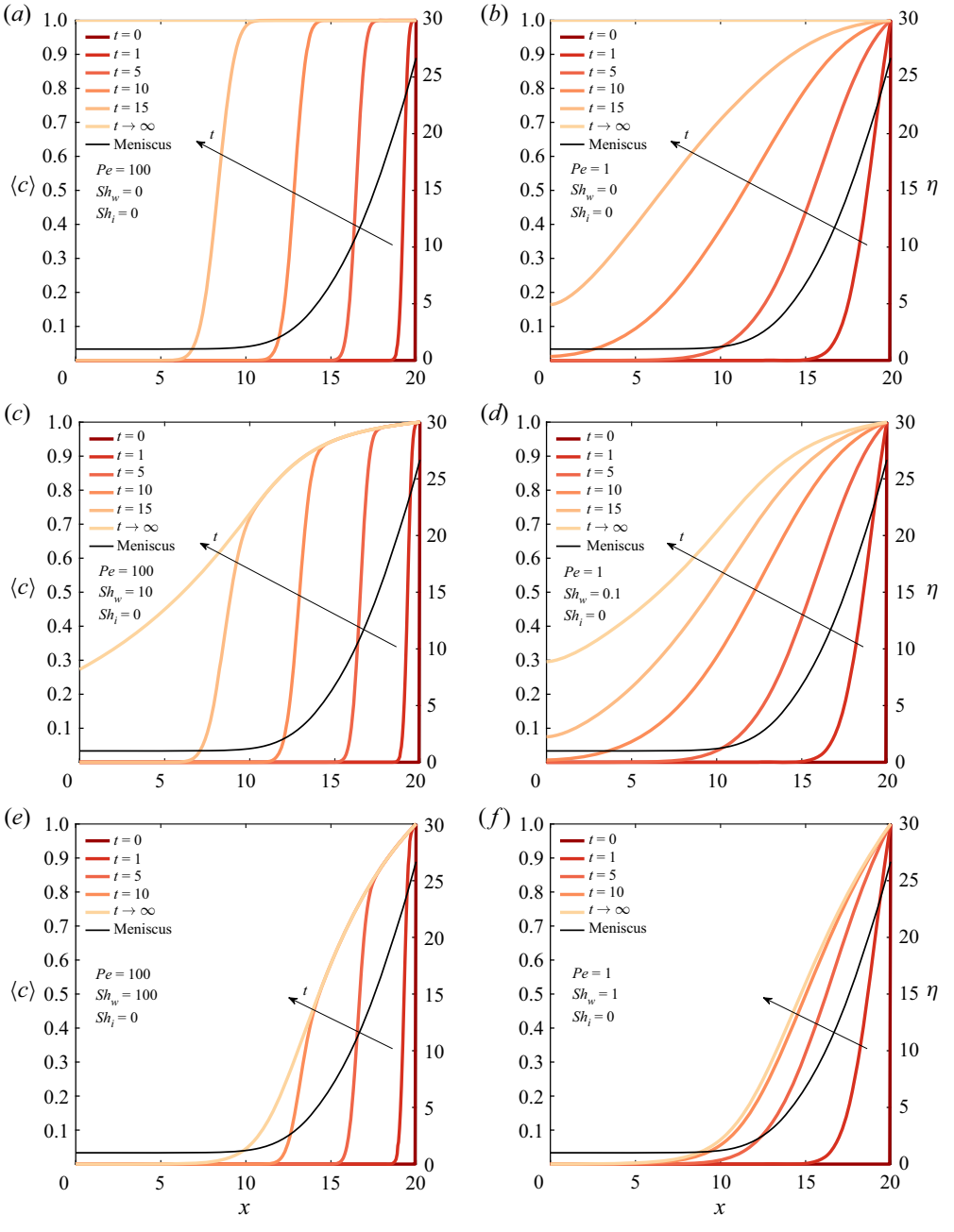

Figure 6. Breakthrough curves for the averaged concentration in the front meniscus as a function of Pe and Sh_w; in all the cases $\varepsilon = 0.01$. On the left of each panel the averaged concentration at different times is plotted, on the right the front meniscus. Cases (a,c,e) are dominated by advection; in (b,d,f) diffusion compete with advection.

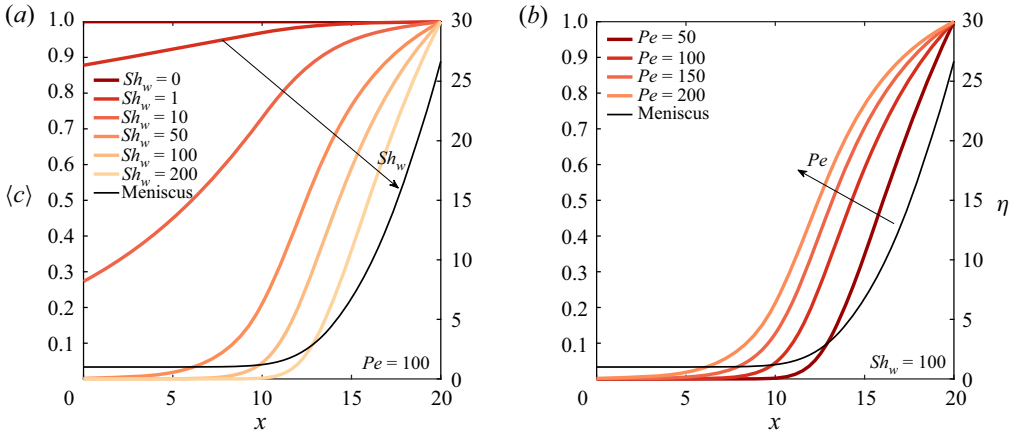

Figure 7. Breakthrough curves for the averaged concentration at the steady state, $\langle c\rangle(x, t \to \infty)$, in the front meniscus. In all the cases $\varepsilon = 0.01$ and $Sh_i = 0$. (*a*) Effect of the Sherwood number; (*b*) effect of the Pèclet number.

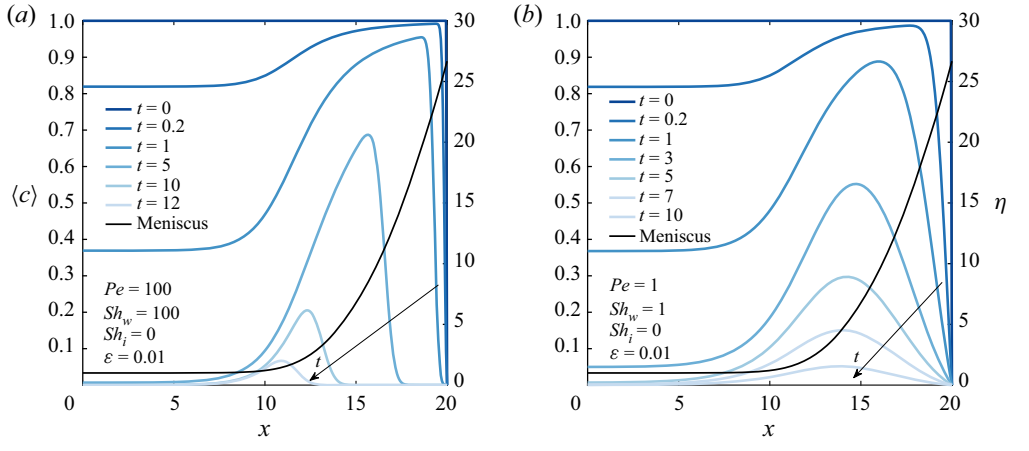

Figure 8. Breakthrough curves during the formation of the hot spot of the average of the concentration, $\langle c\rangle(x, t)$, for (*a*) regime I and (*b*) regime III. See online supplementary Movies 2 and 3 for simulations of these cases.

initialise the simulations imposing a concentration field $\langle c\rangle(x, 0) = 1$ in the entire fluid domain and $\langle c\rangle(x_0, t) = 0$ at the right boundary of the domain.

Figure 8(*a*) shows a significant case where the formation of a hot spot can be observed in the advection dominated regime ($Pe = Sh_w = 100$). At early times, $t = 0.2$, the concentration starts decaying in the fluid domain due to surface mass transfer according to the magnitude of $Sh^\star$, see figure 4(*c*). The solute is quickly consumed in the uniform film region (where $Sh^\star$ is maximum) while it is mainly advected into the parabolic region of the front meniscus (where $u^\star$ is maximum and $Sh^\star \approx 0$). Since the effective velocity vanishes in the uniform film, an accumulation of solute forms. Finally, at later times, the hot spot is consumed by the surface mass transfer.

The hot spot is the result of the transition between the parabolic region, where the effective velocity dominates, and the uniform film, where the effective mass transfer dominates over the advection coefficient. The formation of the hot spot is observed only

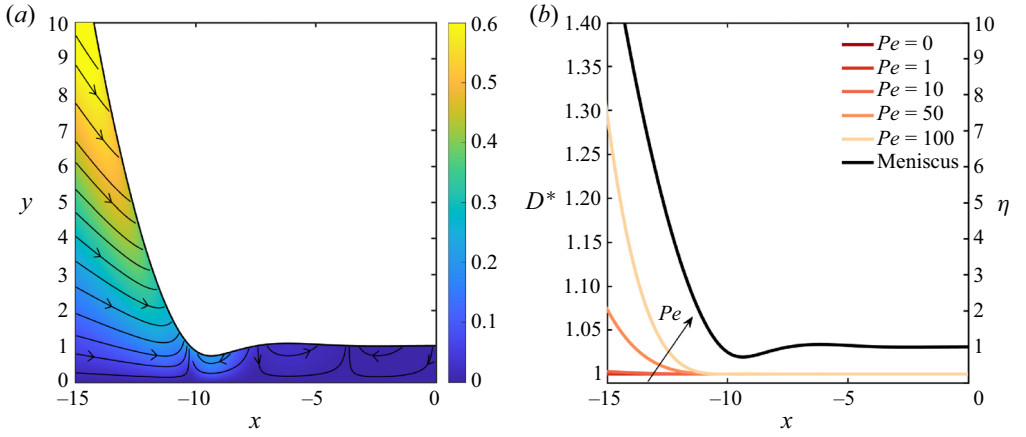

Figure 9. (*a*) Contours of the magnitude of the velocity, $\sqrt{u(x,y)^2 + v(x,y)^2}$ and flow streamlines with respect to a fixed reference frame in the bubble rear. (*b*) Effective diffusion coefficient as function of Pe in the rear meniscus; the scale parameter is set to $\varepsilon = 0.01$.

when the Pèclet number balances with the Sherwood number, i.e. $Pe \sim Sh_w$, otherwise one of the two mechanisms prevails. A similar behaviour occurs for $Pe = Sh_w = 1$, as shown in figure 8(*b*) and in supplementary Movies 2 and 3.

3.2. *The concentration field in the rear meniscus*

In this section, we investigate how the solute is transported in the rear of the bubble. Differently from the front, the meniscus shows the typical oscillations and, therefore, the effective coefficients in (2.19) are non-monotonic with respect to x.

The effective diffusion coefficient $D^\star$, is marginally influenced by the oscillations and the enhancement due to shear flow is significant only far from the uniform film, see figure 9(*b*). Specifically, the shape oscillations induce changes in the sign of the driving force (when $\eta < 1$ then $\mathrm{d}p/\mathrm{d}x > 0$ while $\eta > 1$ gives $\mathrm{d}p/\mathrm{d}x < 0$) and regions of backflow appear. This leads to the formation of recirculating vortices in the bubble rear (see the streamlines in figure 9*a*) and the effective velocity changes sign in correspondence of such oscillations. The evolution of $u^\star$ is presented in figure 10 where we can observe that the effect of Pe and Sh_i on the effective velocity is negligible.

The presence of the recirculating vortices drives the evolution of the effective Sherwood number. Differently from the bubble front, where $Sh^\star$ is maximal in the uniform film region, in the rear, mass transfer is locally enhanced in proximity to the minimum of the bubble profile, see figure 10(*c*). There, a recirculating vortex forms and tends to squeeze out the liquid from the narrow film (see the streamlines in figure 9*a*). The scalar is concentrated in a narrow gap in proximity to the boundaries, enhancing the mass-transfer mechanism. This effect is more pronounced as Sh_w (or Sh_i) increases.

The fact that shape oscillations enhance mass transfer at the bubble–fluid interface is a known phenomenon for the case of unconfined bubbles (Beek & Kramers 1962; Angelo, Lightfoot & Howard 1966) and this seems to be confirmed for the case of Taylor bubbles. Hayashi *et al.* (2014) demonstrated that fluctuations of the bubble surface area at the bubble rear account for the main contribution to the oscillation of the effective Sherwood number. The authors arrived at this conclusion after an analysis of the velocity and the

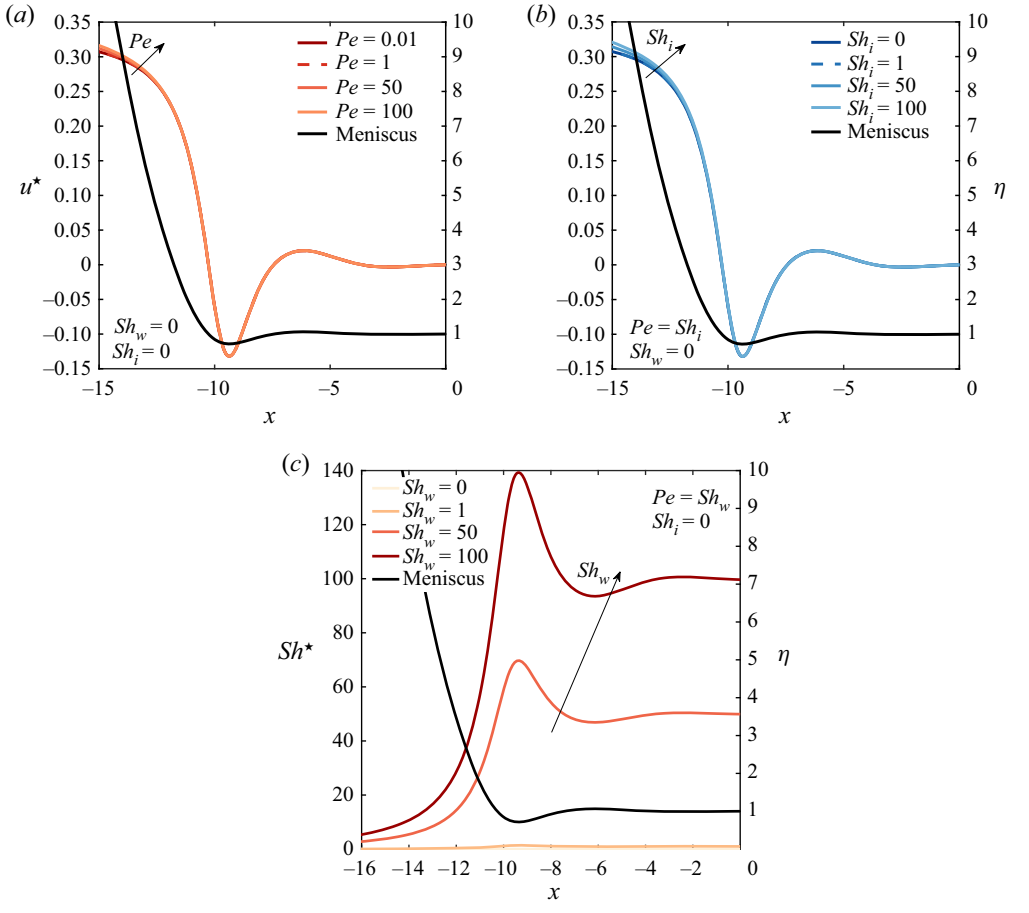

Figure 10. Effective velocity in the rear meniscus as a function of Pe, (a) and Sh_i, (b). (c) Effective mass-transport coefficient in the rear meniscus as a function of Sh_w; the evolution of Sh_i is not shown since there is no discernible difference in plotting $Sh^\star$. In all cases the scale parameter is set to $\varepsilon = 0.01$.

concentration fields around a Taylor bubble rising in a microchannel. Our theoretical results support this evidence.

Figure 11 shows the time evolution of the averaged concentration in the bubble rear for the advection dominated regime with $Pe = 100$, $Sh_w = 10$ and $Sh_i = 0$. The case has been constructed solving (2.19) with initial concentration $\langle c\rangle(x, 0) = 0$ in the entire domain and $\langle c\rangle(0, t) = 1$ at the right boundary of the domain. The concentration front is sharp at $t = 1$, see figure 11(a), and it gets more and more diffuse at later times, see figure 11(d). As the front moves away from the uniform film region, the concentration progressively decays as an effect of the surface mass-transfer mechanism; the breakthrough curves for this case are presented in figure 12(c). The movie of this case is available as supplementary Movie 5.

When the surface mass-transfer mechanism is augmented to $Sh_w = Pe = 100$, the decay of the solute is more intense and the concentration front cannot escape the film region, figure 12(e). On the other hand, if mass transfer is turned off, $Sh_w = 0$, the front advances towards the bubble rear almost undisturbed, figure 12(a).

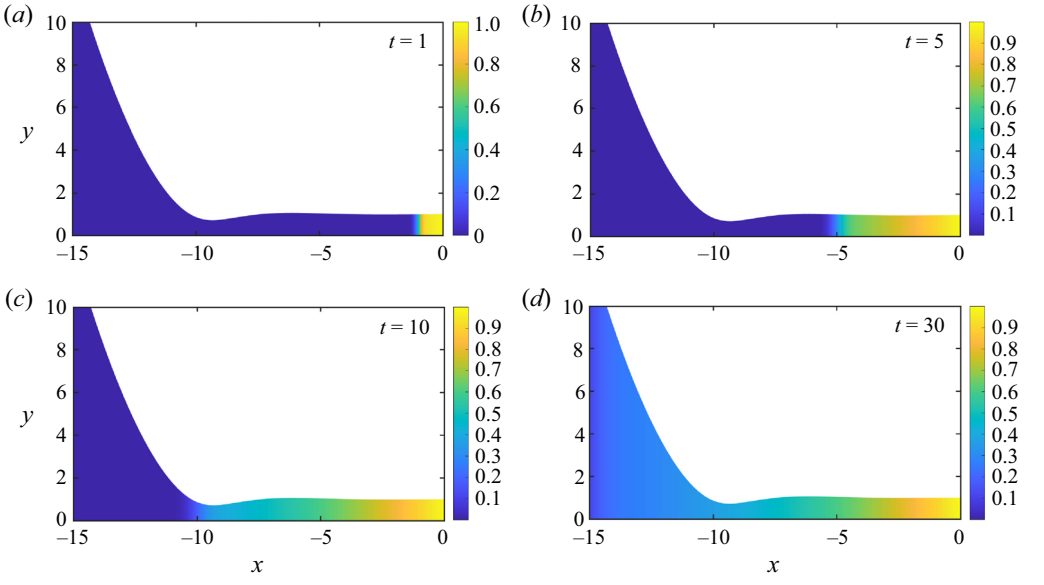

Figure 11. Time evolution of the average of the concentration, $\langle c\rangle(x,t)$, for $Pe = 100$, $Sh_w = 10$, $Sh_i = 0$ and $\varepsilon = 0.01$. Note that the quantity plotted is a one-dimensional approximation of a two-dimensional field. See online supplementary Movie 5 for a simulation of this case.

When diffusion and advection compete for $Pe = 1$, the front is rapidly diffused and, as Sh_w increases, the concentration decay in the film region becomes more intense. The effect of the Sherwood number is presented in figure 12(b,d,f). In this regime, when $Pe \sim Sh_w$, the solute is consumed before exiting the uniform film region, figure 12(f).

3.3. *The concentration field in the uniform film*

In this section, we study the mechanisms that govern the transport problem in the uniform film region, i.e. where $\eta = 1$ and $\mathrm{d}\eta/\mathrm{d}x = 0$ in figure 1. In this region, the fluid is at rest since the curvature is infinite and consequently $\mathrm{d}p/\mathrm{d}x = 0$, see (A6). The advection–diffusion–mass-transfer equation (2.19) reduces to

$$\frac{\partial\langle c\rangle}{\partial t} - \frac{\partial\langle c\rangle}{\partial x} + \frac{Sh_f^\star}{Pe}\langle c\rangle = \frac{1}{Pe}\frac{\partial^2\langle c\rangle}{\partial x^2}, \tag{3.2}$$

where

$$Sh_f^\star = Sh_w + Sh_i + \frac{\varepsilon^2}{3}(Sh_w\, Sh_i - Sh_w^2 - Sh_i^2). \tag{3.3}$$

Differently from the general case, the effective velocity is identically zero, $u_f^\star = 0$, and the effective diffusion coefficient is equal to unity, $D_f^\star = 1$. The concentration distribution is controlled by the competition between diffusion and superficial mass transfer, while the advection term in (3.2) is there only because we consider a reference frame attached to the bubble. In the film, the effective Sherwood number $Sh_f^\star$ does not depend on the bubble geometry and, therefore, it is representative of the total mass transfer.

The main advantage in studying the transport problem in the uniform film region is that (3.2) admits analytical solutions. In fact, the desired solution can be constructed from the

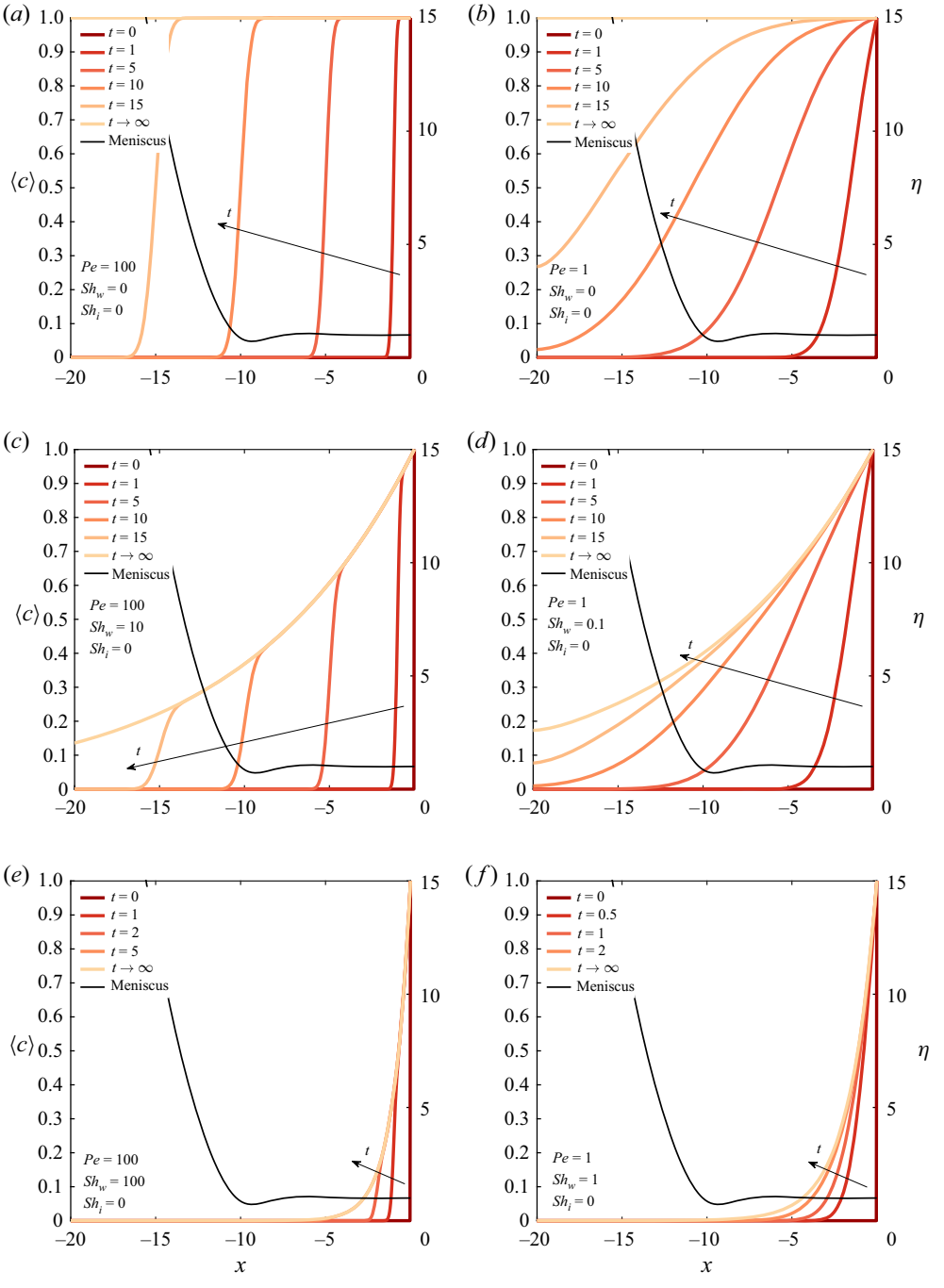

Figure 12. Breakthrough curves for the averaged concentration in the rear meniscus as a function of Pe and Sh_w; in all the cases $\varepsilon = 0.01$. On the left of each panel the averaged concentration at different times is plotted, on the right the rear meniscus. Cases (a,c,e) are dominated by advection; in (b,d,f) advection competes with diffusion.

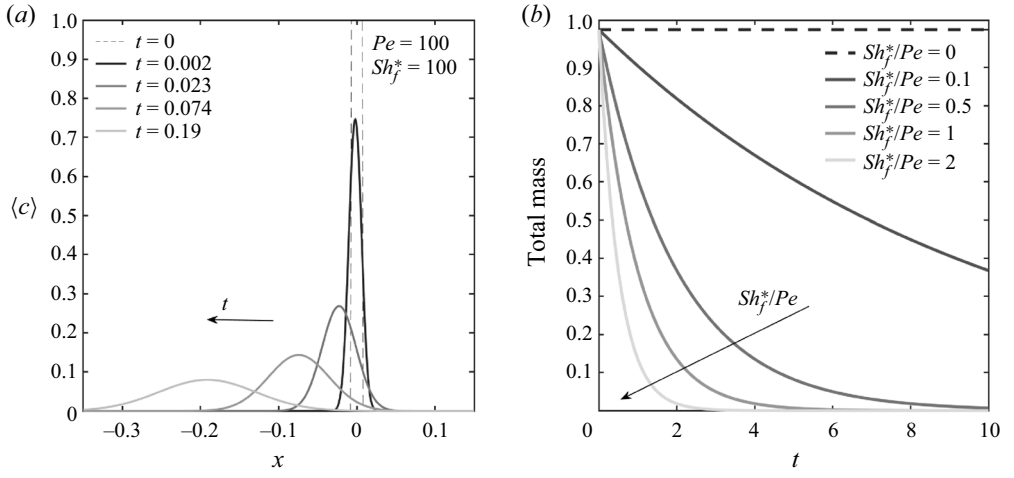

Figure 13. (*a*) Evolution of the averaged concentration in response to a pulse of height equal to unity, centred at $x = 0$. (*b*) Decay of the total mass as a function of time and the ratio $Sh_f^\star/Pe$.

following Green function (i.e. the solution to a point-source initial condition centred at $x = 0$):

$$\mathcal{G}(x,t) = \frac{\exp\left(-\dfrac{Sh_f^\star}{Pe}t\right)}{\sqrt{4\pi t/Pe}} \exp\left(-\frac{(x-t)^2}{4t/Pe}\right). \tag{3.4}$$

Since the Green function is general and it is applicable to different sets of initial and boundary conditions, we focus on the study of a simplified case. We solve (3.2) initialising the concentration film with a pulse of height equal to unity, centred at $x = 0$, in a regime where advection dominates over diffusion, $Pe = 100$, and competes with superficial mass transfer, $Sh_f^\star = 100$. The solution is a Gaussian function that diffuses and decays in time while being advected along x, as shown in figure 13(*a*). Interestingly, the total mass, i.e.

$$\int_{-\infty}^{\infty} \mathcal{G}(x,t)\,\mathrm{d}x = \exp\left(-\frac{Sh_f^\star}{Pe}t\right), \tag{3.5}$$

exponentially decays, controlled by the competition between $Sh_f^\star$ and Pe. Specifically, when $Sh_f^\star/Pe \to 0$, axial diffusion has an effect only on the concentration maximum, but the total mass remains constant. When $Sh_f^\star/Pe$ is finite, instead, the total mass diminishes, as shown in figure 13(*b*) and the residence time of the solute in the uniform film gets progressively shorter (it scales as Pe/Sh_f).

The analytical solution of the transport problem in the uniform film can be employed in the construction of mechanistic or more sophisticated models where knowing the spatial and time evolution of the concentration field is of interest.

4. Conclusions

In this paper, we studied the transport of a passive scalar around a confined Taylor bubble in the presence of surface mass transfer. We derived a one-dimensional

advection–diffusion–mass-transfer equation that applies to the front and rear menisci of the bubble. Specifically, advection, diffusion and superficial mass-transfer mechanisms are described through an effective velocity, effective diffusion and effective mass-transfer coefficients, expressed analytically as a function of the Pèclet and Sherwood numbers, and the film thickness. Our analysis helped in quantifying the contributions that shear flow in the film, changes in the meniscus shape and the presence of mass transfer at the domain boundaries make to the effective coefficients.

Concerning the bubble front, shear flow in the film acts to smear out the concentration distribution in the axial direction, enhancing the effective diffusion coefficient at sufficiently large Pèclet number. Interestingly, the diffusion coefficient scales with the square of the film Pèclet number, recovering the same scaling law typical of the of Aris–Taylor dispersion. Superficial mass transfer is maximum in the uniform film region, where the fluid is at rest and the solute is rapidly consumed. Also, there exist regimes where the solute is entirely consumed even before reaching the uniform film region and, when the Pèclet number balances with the Sherwood number, there exists the condition that leads to the formation of hot spots of concentration around the nose of the bubble.

The analysis of the transport problem in the bubble rear reveals that the mass transfer is locally enhanced in correspondence with the typical meniscus oscillations. There, the presence of recirculating vortices enhances the solute availability for superficial mass transfer. The analysis of the uniform film region is facilitated since the analytical solution can be obtained starting from Green functions of the presented advection–diffusion–mass-transfer equation.

Despite the fact that the motivation of our work is oriented to microfluidics applications that involve solute transport and mass transfer, its ramifications are relevant also in scenarios where the presence of a solute affects the surface tension (i.e. Marangoni effect) or even drives the flow (i.e. diffusioosmosis). In fact, cases where the gradient in the concentration of colloidal particles spontaneously drives the flow are typical of emerging fields, such as micro-filtration and bio-medical engineering: an understanding of those coupling mechanisms in the surroundings of elongated bubbles could be of help for the design of such applications. Thanks to the similar mathematical structure, the results obtained may also offer a new interpretation of heat transfer in the proximity of the Taylor bubble. More generally, several practical problems that involve thin films share a lot of similarities from a fluid mechanics perspectives (Stone 2010), and, therefore, the proposed model may serve as a starting step to generalise the well-known Landau–Levich–Derjaguin–Bretherton problem in the presence of an active scalar.

Supplementary movies. Supplementary movies are available at https://doi.org/10.1017/jfm.2022.829.

Acknowledgements. We a thank the anonymous reviewers for their careful reading of our manuscript and their many insightful comments and suggestions.

Declaration of interests. The authors report no conflict of interest.

Author ORCIDs.
D. Picchi https://orcid.org/0000-0002-2619-104X.

Appendix A. Velocity profiles in the film region

According to Bretherton (1961), the flow in the film region is expressed using a lubrication approximation. Specifically, the velocity in the axial direction is a free-surface velocity

profile given by

$$\hat{u}(\hat{x},\hat{y}) = \frac{\mathrm{d}\hat{p}}{\mathrm{d}\hat{x}}\frac{(\hat{y}^2 - 2\hat{h}\hat{y})}{2\mu}. \tag{A1}$$

The velocity in the transverse direction can be obtained starting from the continuity equation

$$\frac{\partial \hat{u}}{\partial \hat{x}} + \frac{\partial \hat{v}}{\partial \hat{y}} = 0, \tag{A2}$$

and integrating over the film

$$\hat{v}(\hat{x},\hat{y}) = -\int_0^{\hat{y}} \frac{\partial \hat{u}}{\partial \hat{x}}\,\mathrm{d}\hat{y} = -\frac{1}{2\mu}\left[\frac{\mathrm{d}^2\hat{p}}{\mathrm{d}\hat{x}^2}\left(\frac{\hat{y}^3}{3} - \hat{h}\hat{y}^2\right) - \frac{\mathrm{d}\hat{p}}{\mathrm{d}\hat{x}}\frac{\mathrm{d}\hat{h}}{\mathrm{d}\hat{x}}\hat{y}^2\right]. \tag{A3}$$

Introducing the definitions of the dimensionless variables defined in (2.3*a–c*), (2.9*a–f*) and using $\sigma\varepsilon^2/h$ as the scale for the pressure, the dimensionless velocity profiles in the x and y directions read

$$u(x,y) = \frac{1}{2}\frac{\mathrm{d}p}{\mathrm{d}x}(y^2 - 2\eta y), \tag{A4}$$

$$v(x,y) = -\frac{1}{2}\left[\frac{\mathrm{d}^2p}{\mathrm{d}x^2}\left(\frac{y^3}{3} - \eta y^2\right) - y^2\frac{\mathrm{d}\eta}{\mathrm{d}x}\frac{\mathrm{d}p}{\mathrm{d}x}\right]. \tag{A5}$$

Expressing the pressure gradient as a function of η using (2.2)

$$\frac{\mathrm{d}p}{\mathrm{d}x} = -\frac{\mathrm{d}^3\eta}{\mathrm{d}x^3} = -\frac{\eta - 1}{\eta^3}, \tag{A6}$$

we obtain

$$u(x,y) = -\frac{\eta - 1}{2\eta^3}(y^2 - 2\eta y), \tag{A7}$$

$$v(x,y) = \frac{3 - 2\eta}{2\eta^4}\left(\frac{y^3}{3} - \eta y^2\right)\frac{\mathrm{d}\eta}{\mathrm{d}x} - y^2\frac{\eta - 1}{2\eta^3}\frac{\mathrm{d}\eta}{\mathrm{d}x}. \tag{A8}$$

Appendix B. Derivation of the transport equation by means of two-scale expansion

In the following sections the derivation of the effective equation for the average concentration is carried out separately for each regime, identified by the magnitude of the Pèclet number.

B.1. *Advection dominated regime, $Pe = O(\varepsilon^{-1})$*

In regimes where $Pe = O(\varepsilon^{-1})$ or $\alpha = 1$, replacing the expanded variables (2.17) and the dimensionless numbers (2.16*a–c*) in the equation for the concentration, (2.10), we obtain

$$\begin{aligned} &-\varepsilon^{\alpha-2}\frac{\partial^2 c_0}{\partial y^2} + \varepsilon^0\left[\frac{\partial c_0}{\partial t} + (u(x,y) - 1)\frac{\partial c_0}{\partial x} + v(x,y)\frac{\partial c_0}{\partial y} - \varepsilon^{\alpha-1}\frac{\partial^2 c_1}{\partial y^2}\right] \\ &+ \varepsilon\left[\frac{\partial c_1}{\partial t} + (u(x,y) - 1)\frac{\partial c_1}{\partial x} + v(x,y)\frac{\partial c_1}{\partial y} - \varepsilon^{\alpha-1}\frac{\partial^2 c_0}{\partial x^2} - \varepsilon^{\alpha-1}\frac{\partial^2 c_2}{\partial y^2}\right] + \ldots = 0, \end{aligned} \tag{B1}$$

where $u(x, y)$ and $v(x, y)$ are given in (A7) and (A8), respectively. Similarly, the expanded boundary conditions, (2.12) and (2.15), yield

$$\frac{\partial c_0}{\partial y} + \varepsilon \frac{\partial c_1}{\partial y} + \varepsilon^2 \frac{\partial c_2}{\partial y} = \varepsilon^{2+\beta} c_0 + \varepsilon^{3+\beta} c_1 + \varepsilon^{4+\beta} c_2 + O(\varepsilon^2) \quad \text{at } y = 0, \tag{B2}$$

$$-\frac{\partial c_0}{\partial y} - \varepsilon \frac{\partial c_1}{\partial y} - \varepsilon^2 \frac{\partial c_2}{\partial y} = \varepsilon^{2+\gamma} c_0 + \varepsilon^{3+\gamma} c_1 + \varepsilon^{4+\gamma} c_2 + O(\varepsilon^2) \quad \text{at } y = \eta. \tag{B3}$$

Collecting the terms at the leading order $O(\varepsilon^{-1})$, we get

$$\left.\begin{aligned} -\frac{\partial^2 c_0}{\partial y^2} &= 0 \quad y \in [0, \eta], \\ \frac{\partial c_0}{\partial y} &= 0 \quad \text{at } y = 0, \\ \frac{\partial c_0}{\partial y} &= 0 \quad \text{at } y = \eta. \end{aligned}\right\} \tag{B4}$$

The homogeneity of the equation and the boundary conditions in (B4) ensure that the boundary-value problem admits a trivial solution (i.e. that c_0 is independent of y), and, therefore, c_0 is the average concentration defined in (2.18), $c_0(x, t) = \langle c \rangle (x, t)$. This is true as long as $\alpha < 2$, $\beta > -2$ and $\gamma > -2$, namely, $Pe \ll O(\varepsilon^{-2})$ and $Sh_w \ll O(\varepsilon^{-2})$ and $Sh_i \ll O(\varepsilon^{-2})$. At the next order, $O(1)$, we obtain the following boundary-value problem:

$$\left.\begin{aligned} -\frac{\partial^2 c_1}{\partial y^2} = -\varepsilon^{1-\alpha} \frac{\partial c_0}{\partial t} - \varepsilon^{1-\alpha} \left[-\frac{\eta - 1}{2\eta^3} \left(y^2 - 2\eta y \right) - 1 \right] \frac{\partial c_0}{\partial x} + v(x, y) \frac{\partial c_0}{\partial y}, \\ \frac{\partial c_1}{\partial y} = \varepsilon^{1+\beta} c_0 \quad \text{at } y = 0, \\ -\frac{\partial c_1}{\partial y} = \varepsilon^{1+\gamma} c_0 \quad \text{at } y = \eta. \end{aligned}\right\} \tag{B5}$$

Since c_0 is independent of y, the last term on the right-hand side of (B5) vanishes, i.e. $\partial c_0 / \partial y = 0$. A necessary condition for the existence of the solution is that the integration of (B5) between $y = 0$ and $y = \eta$ with the use of its boundary conditions is identically zero. This condition is known in the literature as the compatibility condition or Fredholm alternative (see e.g. Rubinstein & Mauri 1986; Auriault 2002; Mikelić *et al.* 2006). Unfortunately, for the problem considered, the initial and boundary data for c_0 are incompatible and, therefore, this procedure leads to a discontinuous solution. This issue can be solved by integrating (B5) between $y = 0$ and $y = \eta$ with the addition of a smaller correction, of the order of ε,

$$\frac{\partial c_0}{\partial t} - \left(-\frac{\eta - 1}{3\eta} + 1 \right) \frac{\partial c_0}{\partial x} + \frac{c_0 \varepsilon^\alpha}{\eta} \left(\varepsilon^\beta + \varepsilon^\gamma \right) = O(\varepsilon). \tag{B6}$$

A similar procedure has been employed in Mikelić *et al.* (2006) and Rubinstein & Mauri (1986). By inspection of (B6) we get an additional constraint on the Pèclet and the Sherwood numbers, i.e. $\alpha + \beta > -1$ and $\alpha + \gamma > -1$ ($Sh_w/Pe \ll O(\varepsilon^{-1})$ and $Sh_i/Pe \ll O(\varepsilon^{-1})$).

Substituting (B6) into (B5), we obtain a boundary-value problem for the computation of $c_1(x, y, t)$

$$\left.\begin{aligned} -\frac{\partial^2 c_1}{\partial y^2} &= \varepsilon^{\alpha-1}\frac{\eta-1}{2\eta^3}\left(y^2-2\eta y+\frac{2}{3}\eta^2\right)\frac{\partial c_0}{\partial x}+\varepsilon\frac{c_0}{\eta}\left(\varepsilon^{\beta}+\varepsilon^{\gamma}\right), \\ \frac{\partial c_1}{\partial y} &= \varepsilon^{1+\beta}c_0 \quad \text{at } y=0, \\ -\frac{\partial c_1}{\partial y} &= \varepsilon^{1+\gamma}c_0 \quad \text{at } y=\eta, \end{aligned}\right\} \tag{B7}$$

whose integration leads to

$$\begin{aligned} c_1(x, y, t) = &-\varepsilon^{1-\alpha}\frac{\eta-1}{2\eta^3}\left(\frac{y^4}{12}-\frac{\eta y^3}{3}+\frac{\eta^2 y^2}{3}\right)\frac{\partial c_0}{\partial x}+\varepsilon\left[\varepsilon^{\beta}\left(y-\frac{y^2}{2\eta}\right)-\varepsilon^{\gamma}\frac{y^2}{2\eta}\right]c_0 \\ &+C_0(x, t), \end{aligned} \tag{B8}$$

where $C_0(x, t)$ is an arbitrary function. To determine $C_0(x, t)$, we impose that c_1 has zero average, namely $\int_0^{\eta} c_1\,\mathrm{d}y = 0$, giving

$$C_0(x, t) = \varepsilon^{1-\alpha}\frac{(\eta-1)\eta}{45}\frac{\partial c_0}{\partial x}-\varepsilon\eta\left(\frac{\varepsilon^{\beta}}{3}-\frac{\varepsilon^{\gamma}}{6}\right)c_0. \tag{B9}$$

Combining (B8) and (B9) we get the final expression for $c_1(x, y, t)$

$$\begin{aligned} c_1 = &-\varepsilon^{1-\alpha}\frac{(\eta-1)}{2\eta^3}\left(\frac{y^4}{12}-\frac{\eta y^3}{3}+\frac{\eta^2 y^2}{3}-\frac{2\eta^4}{45}\right)\frac{\partial c_0}{\partial x} \\ &+\varepsilon\left[\varepsilon^{\beta}\left(y-\frac{y^2}{2\eta}-\frac{\eta}{3}\right)+\varepsilon^{\gamma}\left(\frac{\eta}{6}-\frac{y^2}{2\eta}\right)\right]c_0. \end{aligned} \tag{B10}$$

Then, we collect the terms of order $O(\varepsilon)$ in (B1), including the additional terms resulting from (B6), and we obtain a boundary-value problem for $c_2(x, y, t)$

$$\left.\begin{aligned} -\frac{\partial^2 c_2}{\partial y^2} = &-\varepsilon^{1-\alpha}\left(u(x, y)-1\right)\frac{\partial c_1}{\partial x}+\frac{\partial^2 c_0}{\partial x^2}-\varepsilon^{1-\alpha}\frac{\partial c_1}{\partial t}-\varepsilon^{1-\alpha}v(x, y)\frac{\partial c_1}{\partial y} \\ &-\varepsilon^{-\alpha}\left[\frac{\partial c_0}{\partial t}-\left(-\frac{\eta-1}{3\eta}+1\right)\frac{\partial c_0}{\partial x}+\varepsilon^{\alpha}\frac{c_0}{\eta}\left(\varepsilon^{\beta}+\varepsilon^{\gamma}\right)\right], \\ \frac{\partial c_2}{\partial y} &= \varepsilon^{1+\beta}c_1 \quad \text{at } y=0, \\ -\frac{\partial c_2}{\partial y} &= \varepsilon^{1+\gamma}c_1 \quad \text{at } y=\eta. \end{aligned}\right\} \tag{B11}$$

Integrating (B11) between $y = 0$ and $y = \eta$ with the use of (A7) and (A8) we get

$$
\begin{aligned}
&-\left.\frac{\partial c_2}{\partial y}\right|_{y=\eta} + \left.\frac{\partial c_2}{\partial y}\right|_{y=0} \\
&\quad = -\varepsilon^{1-\alpha}\int_0^{\eta}\left[-\frac{\eta-1}{2\eta^3}(y^2-2\eta y)-1\right]\frac{\partial c_1}{\partial x}\mathrm{d}y + \int_0^{\eta}\frac{\partial^2 c_0}{\partial x^2}\,\mathrm{d}y \\
&\qquad - \varepsilon^{1-\alpha}\int_0^{\eta}\frac{\partial c_1}{\partial t}\mathrm{d}y - \varepsilon^{1-\alpha}\int_0^{\eta}\frac{1}{2}\left[\frac{3-2\eta}{\eta^4}\frac{\mathrm{d}\eta}{\mathrm{d}x}\left(\frac{y^3}{3}-\eta y^2\right) - y^2\frac{\eta-1}{\eta^3}\frac{\mathrm{d}\eta}{\mathrm{d}x}\right]\frac{\partial c_1}{\partial y}\,\mathrm{d}y \\
&\qquad - \varepsilon^{-\alpha}\int_0^{\eta}\left[\frac{\partial c_0}{\partial t} - \left(-\frac{\eta-1}{3\eta}+1\right)\frac{\partial c_0}{\partial x} + \varepsilon^{\alpha}\frac{c_0}{\eta}\left(\varepsilon^{\beta}+\varepsilon^{\gamma}\right)\right]\mathrm{d}y. \qquad \text{(B12)}
\end{aligned}
$$

The integrals in (B12) are carried out recalling that $c_0(x, t)$ is independent of y, using the full expression of $c_1(x, y, t)$ given in (B10), and the relation

$$
\int_0^{\eta(x)}\frac{\partial c_1}{\partial t}\mathrm{d}y = \frac{\partial}{\partial t}\int_0^{\eta(x)} c_1\,\mathrm{d}y = 0, \qquad \text{(B13)}
$$

since $\eta(x)$ does not depend upon time and $c_1(x, y, t)$ has zero average. Using the boundary conditions from (B11) to replace the left-hand side of (B12), we get the following conservation equation for the leading-order c_0 (or the averaged concentration):

$$
\begin{aligned}
&\frac{\partial c_0}{\partial t} + \left[\frac{\eta-1}{3\eta} - \varepsilon^{2-\alpha}\frac{(73\eta-8)(\eta-1)}{3780\eta}\frac{\mathrm{d}\eta}{\mathrm{d}x} - \varepsilon^{2+\gamma}\frac{14\eta(\eta-1)+(73\eta+47)\,\mathrm{d}\eta/\mathrm{d}x}{360\eta}\right. \\
&\qquad \left. + \varepsilon^{2+\beta}\frac{16\eta(\eta-1)+(47\eta+13)\,\mathrm{d}\eta/\mathrm{d}x}{360\eta} - 1\right]\frac{\partial c_0}{\partial x} \\
&\qquad + \left[\varepsilon^{\alpha}\frac{\varepsilon^{\beta}+\varepsilon^{\gamma}}{\eta} + \frac{\varepsilon^{2+\alpha}}{3}(\varepsilon^{\beta+\gamma}-\varepsilon^{2\beta}-\varepsilon^{2\gamma})\right. \\
&\qquad \left. - \left(\frac{\varepsilon^{2+\gamma}(7\eta-18)+\varepsilon^{2+\beta}(7-3\eta)}{120\eta}\right)\frac{\mathrm{d}\eta}{\mathrm{d}x}\right]c_0 \\
&\quad = \varepsilon^{\alpha}\left[1+\varepsilon^{2-2\alpha}\frac{2(\eta-1)^2}{945}\right]\frac{\partial^2 c_0}{\partial x^2}. \qquad \text{(B14)}
\end{aligned}
$$

Advection, superficial mass transfer and diffusion are accounted for through effective coefficients. In this regime, transverse advection affects both the effective advection and the effective mass-transfer terms, while the effective diffusion is driven by the flow in the axial direction only. Equation (B14) represents the generalisation of the Aris–Taylor dispersion to the film region of a Taylor bubble.

Note that the effective equation (B14) converges to the results obtained by Mikelić *et al.* (2006) when (i) advection balances with interfacial mass transfer at the wall $O(Pe) = O(Sh_w) = O(\varepsilon^{-1})$ (or $\beta + \alpha = 0$ with $\alpha = 1$); (ii) mass transfer at the interface is negligible; (iii) the interface is flat like in the case of a straight channel ($\eta = 1$) and we use back (A6) to restore the $\mathrm{d}p/\mathrm{d}x$ term; (iv) we look at the problem in a fixed reference frame. Also, if both mass-transfer mechanisms are turned off, we recover the classical Aris–Taylor dispersion equation (Taylor 1953; Aris 1956).

For the sake of completeness, the second-order correction c_2 can be determined by solving (B11) and choosing that $\int_0^{\eta} c_2\,\mathrm{d}y = 0$. We do not report here the final expression

since we are primarily interested in the evolution of the averaged concentration. As is shown in Appendix D, the first-order correction is negligible within the region of applicability of the model.

B.2. *Competition between advection and diffusion, Pe = O(1)*

In regimes where advection competes with diffusion for $Pe = O(1)$ or $\alpha = 0$, the expanded equation yields

$$-\varepsilon^{\alpha-2}\frac{\partial^2 c_0}{\partial y^2} - \varepsilon^{\alpha-1}\frac{\partial^2 c_1}{\partial y^2} + \frac{\partial c_0}{\partial t} + (u(x,y)-1)\frac{\partial c_0}{\partial x} + v(x,y)\frac{\partial c_0}{\partial y} - \varepsilon^{\alpha}\frac{\partial^2 c_2}{\partial y^2} - \varepsilon^{\alpha}\frac{\partial^2 c_0}{\partial x^2} + \ldots = 0. \tag{B15}$$

Collecting the terms at the leading orders, $O(\varepsilon^{-2})$ and $O(\varepsilon^{-1})$, in (B15) and (B2) we get following boundary-value problems:

$$\left.\begin{aligned} -\frac{\partial^2 c_0}{\partial y^2} &= 0 \quad y \in [0,\eta], \\ \frac{\partial c_0}{\partial y} &= 0 \quad \text{at } y = 0, \\ \frac{\partial c_0}{\partial y} &= 0 \quad \text{at } y = \eta, \end{aligned}\right\} \qquad \left.\begin{aligned} -\frac{\partial^2 c_1}{\partial y^2} &= 0 \quad y \in [0,\eta], \\ \frac{\partial c_1}{\partial y} &= 0 \quad \text{at } y = 0, \\ \frac{\partial c_1}{\partial y} &= 0 \quad \text{at } y = \eta, \end{aligned}\right\} \tag{B16a,b}$$

that ensure that both $c_0(x,t)$ and $c_1(x,t)$ are independent of y. This is true as long as $\beta \geqslant 0$ and $\gamma \geqslant 0$. At the next order, $O(1)$, we obtain

$$\left.\begin{aligned} -\frac{\partial^2 c_2}{\partial y^2} &= -\varepsilon^{-\alpha}\left[\frac{\partial c_0}{\partial t} + (u(x,y)-1)\frac{\partial c_0}{\partial x} + v(x,y)\frac{\partial c_0}{\partial y}\right] + \frac{\partial^2 c_0}{\partial x^2}, \\ \frac{\partial c_2}{\partial y} &= \varepsilon^{1+\beta} c_0 \quad \text{at } y = 0, \\ -\frac{\partial c_2}{\partial y} &= \varepsilon^{1+\gamma} c_0 \quad \text{at } y = \eta. \end{aligned}\right\} \tag{B17}$$

Integrating (B17) between $y = 0$ and $y = \eta$ we obtain

$$-\left.\frac{\partial c_2}{\partial y}\right|_{y=\eta} + \left.\frac{\partial c_2}{\partial y}\right|_{y=0} = -\varepsilon^{-\alpha}\left[\int_0^\eta \frac{\partial c_0}{\partial t}\,\mathrm{d}y + \int_0^\eta (u(x,y)-1)\frac{\partial c_0}{\partial x}\,\mathrm{d}y + \int_0^\eta v(x,y)\frac{\partial c_0}{\partial y}\,\mathrm{d}y\right] + \int_0^\eta \frac{\partial^2 c_0}{\partial x^2}\,\mathrm{d}y. \tag{B18}$$

Using the boundary conditions to replace the left-hand side of (B18), the full expression of $u(x,y)$ given in (A7) and recalling that $c_0(x,t)$ is independent of y, we get the following conservation equation for the averaged concentration:

$$\frac{\partial c_0}{\partial t} + \left(\frac{\eta-1}{3\eta} - 1\right)\frac{\partial c_0}{\partial x} + \varepsilon^{\alpha}\frac{\varepsilon^{\beta}+\varepsilon^{\gamma}}{\eta}c_0 = \varepsilon^{\alpha}\frac{\partial^2 c_0}{\partial x^2}. \tag{B19}$$

In this regime, the contribution of the transverse advection vanishes since $\partial c_0/\partial y = 0$ in (B18) and the diffusive term is limited to molecular diffusion only.

By inspection of (B14) and (B19) we can observe that the solution obtained previously for the advection dominated regime embeds the solution obtained in this section for regimes where advection and diffusion compete. Specifically, when $\alpha = 1$, several terms in (B14) become small and (B14) reduces to (B19).

B.3. *Diffusion dominated regime, $Pe = O(\varepsilon)$ or smaller*

When the Pèclet number is small, $Pe = O(\varepsilon)$ or smaller, diffusion dominates over advection and the relevant time scale is the diffusive time scale instead of the advective one used in (2.9*a–f*). In this case, the same procedure described in previous sections can be applied, provided that the time variable in (2.10) is rescaled as follows:

$$\frac{\partial c}{\partial t} \to \varepsilon^{\alpha} \frac{\partial c}{\partial t_d}, \tag{B20}$$

where $t_d = \hat{t}/\tau_d$ is the dimensionless diffusion time. Plugging the rescaled time variable into (2.10), after doing the expansions, we get the following cascade of equations:

$$-\varepsilon^{\alpha-2}\frac{\partial^2 c_0}{\partial y^2} - \varepsilon^{\alpha-1}\frac{\partial^2 c_1}{\partial y^2} + \varepsilon^{\alpha}\left(\frac{\partial c_0}{\partial t_d} - \frac{\partial^2 c_2}{\partial y^2} - \frac{\partial^2 c_0}{\partial x^2}\right) + \ldots = 0, \tag{B21}$$

coupled with the boundary conditions (B2). It is straightforward to show that this procedure leads to the following diffusion–mass-transfer equation:

$$\frac{\partial c_0}{\partial t_d} + \frac{\varepsilon^{\beta} + \varepsilon^{\gamma}}{\eta} c_0 = \frac{\partial^2 c_0}{\partial x^2}, \tag{B22}$$

provided that $\alpha \leqslant -1$, $\alpha + \beta = 0$ and $\alpha + \gamma = 0$. In this regime, the effect of advection (in both directions) is negligible. If we switch back to the advective time, (B22) is identical to (B19) once we drop the advective term

$$\frac{\partial c_0}{\partial t} + \varepsilon^{\alpha}\frac{\varepsilon^{\beta} + \varepsilon^{\gamma}}{\eta} c_0 = \varepsilon^{\alpha}\frac{\partial^2 c_0}{\partial x^2}. \tag{B23}$$

Therefore, the effective advection–diffusion–mass-transfer equation (B14) embeds all three regimes considered.

Appendix C. Further analysis of the effective velocity and the effective Sherwood number

In this section, we study the relative importance of the different terms appearing in the effective velocity (2.20) and the effective Sherwood number (2.21). If we define

$$\left.\begin{gathered}
\mathcal{I}_1 = \frac{\eta - 1}{3\eta}, \quad \mathcal{I}_2 = -\varepsilon^2 Pe\,\frac{(73\eta - 8)(\eta - 1)}{3780\eta}\frac{\mathrm{d}\eta}{\mathrm{d}x}, \\
\mathcal{I}_3 = \varepsilon^2\left[Sh_i\frac{14\eta(\eta-1) + (73\eta + 47)\,\mathrm{d}\eta/\mathrm{d}x}{360\eta} - Sh_w\frac{16\eta(\eta-1) + (47\eta + 13)\,\mathrm{d}\eta/\mathrm{d}x}{360\eta}\right], \\
\mathcal{M}_1 = \frac{Sh_w + Sh_i}{\eta}, \quad \mathcal{M}_2 = \frac{\varepsilon^2}{3}(Sh_w\,Sh_i - Sh_w^2 - Sh_i^2), \\
\mathcal{M}_3 = -\varepsilon^2 Pe\frac{Sh_i(7\eta - 18) + Sh_w(7 - 3\eta)}{120\eta}\frac{\mathrm{d}\eta}{\mathrm{d}x},
\end{gathered}\right\} \tag{C1}$$

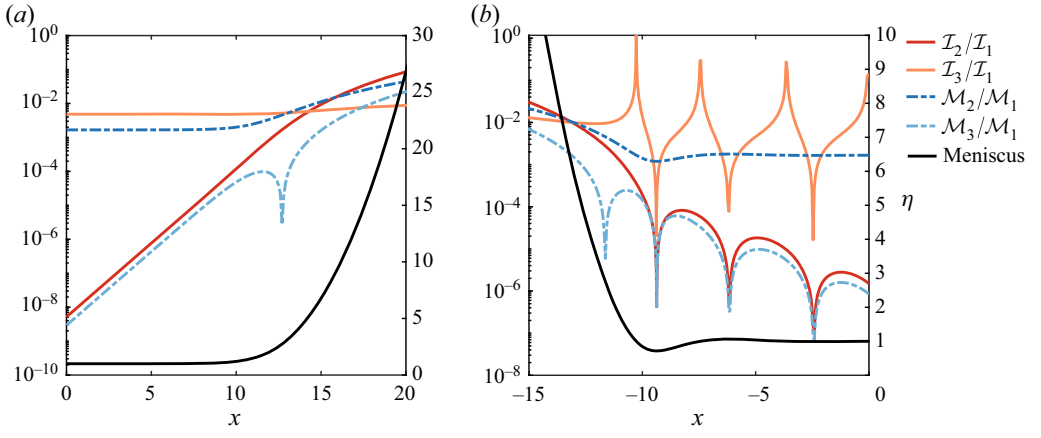

Figure 14. Relative importance of the different terms appearing in $u^\star$, (2.20), and $Sh^\star$, (2.21), for regime I, i.e. $Pe = Sh_w = Sh_i = \varepsilon^{-1}$ and $\varepsilon = 0.01$. (*a*) Bubble front; (*b*) bubble rear.

we can compute the relative importance of the different terms with respect to the dominant one, i.e. $\mathcal{I}_2/\mathcal{I}_1$ and $\mathcal{I}_3/\mathcal{I}_1$ for $u^\star$, and $\mathcal{M}_2/\mathcal{M}_1$ and $\mathcal{M}_3/\mathcal{M}_1$ for $Sh^\star$, respectively. We plot such ratios referring to the most general case where $Pe = Sh_w = Sh_i = O(\varepsilon^{-1})$ (regime I) in figure 14(*a*). Clearly, the terms $\mathcal{I}_2$ and $\mathcal{I}_3$ (which represent the contribution of transverse velocity and superficial mass transfer to the overall effective advection) are negligible compared with $\mathcal{I}_1$ (which represents the contribution of axial velocity only). This is true also in the bubble rear; the spikes in figure 14(*b*) originate from division by zero when $\eta = 1$, but, at such points, $u^\star \approx 0$. Similarly, the terms $\mathcal{M}_2$ and $\mathcal{M}_3$ are much smaller with respect to $\mathcal{M}_1$ in both the front and rear menisci.

From the practical point of view, in the region of validity of the model (see § 2.4), we can approximate the effective coefficients as

$$u^\star \approx \frac{\eta - 1}{3\eta} \quad Sh^\star \approx \frac{Sh_w + Sh_i}{\eta}. \tag{C2a,b}$$

Appendix D. First-order corrections of the concentration field

In § 3.1 we focused on the time evolution of the averaged concentration, that is, in the asymptotic expansion (2.17), the zeroth-order term. For the sake of completeness, we study the concentration field including corrections up to the first order, i.e. $c(x, y, t) = c_0(x, t) + \varepsilon c_1(x, y, t)$. Once $c_0(x, t)$ is known by solving (2.19), the first-order term $\varepsilon c_1(x, y, t)$ can be computed directly from (B10).

To prove that, within the region of applicability of the model (see figure 2) the first-order correction is small, we analyse the order of magnitude of the correction, estimated as

$$O(\varepsilon c_1) = O(\varepsilon^2 Pe\, \eta^2)\frac{\partial c_0}{\partial x} + O(\varepsilon^2 (Sh_w + Sh_i)\eta) c_0. \tag{D1}$$

The axial derivative term in (D1) is controlled by the competition between the Pèclet number and the bubble shape, while the second term vanishes only when surface mass transfer is absent or negligible. When Pe is equal to or smaller than $O(\varepsilon^{-1})$, the axial derivative term does not exceed $O(\varepsilon\eta^2)$. Similarly, when Sh_w or Sh_i is smaller than or equal to $O(\varepsilon^{-1})$, the second term does not exceed $O(\varepsilon\eta)$. Therefore, for all the regimes

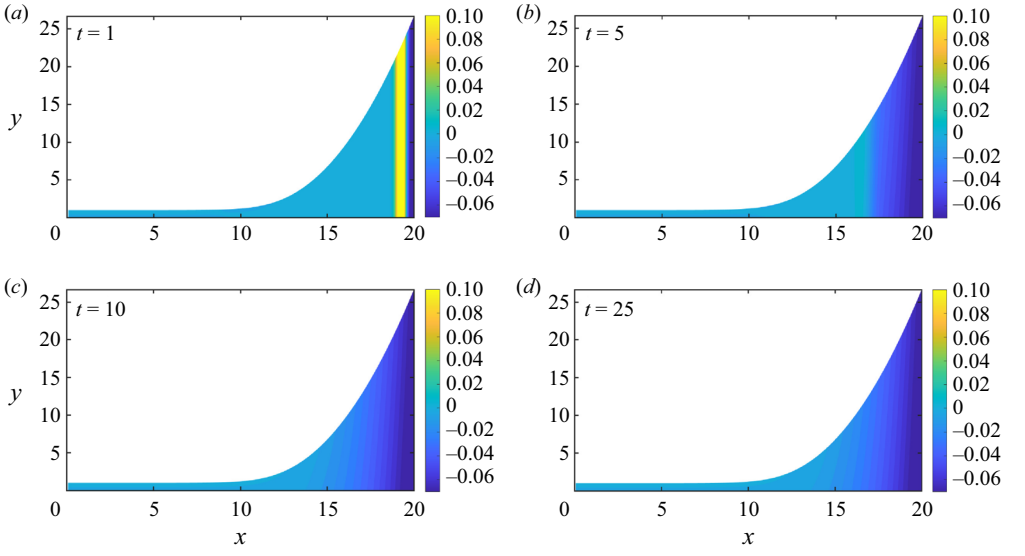

Figure 15. Time evolution of the first-order correction term $\varepsilon c_1(x, y, t)$ in the expansion (2.17) for regime I, i.e. $Pe = 100$, $Sh_w = 100$, $Sh_i = 0$ and $\varepsilon = 0.01$. See also online supplementary Movie 4 for a simulation of this case.

classified in § 2.5, it is reasonable to neglect high-order terms and to look only at the evolution of the averaged concentration.

Figure 15 shows the time evolution of $\varepsilon c_1(x, y, t)$ for the same case depicted in figure 5 corresponding to regime I in figure 2. At early times, the correction is around 10 % only in the proximity of the concentration front, but it becomes negligible when the front has been diffused. As expected, the axial derivative of c_0 contributes only in proximity to sharp variations of the concentration field.

The scenario changes dramatically when the model is brought closer to or out of its validity range. If $Pe = O(\varepsilon^{-2})$, the axial derivative term becomes at least of order one; the same happens for the second term if the Sherwood numbers are of order ε^{-2}. Although the model is not strictly applicable under such conditions, using the model closer to or outside of its theoretical limits would require consideration of higher-order corrections instead of the zeroth-order dynamics only.

References

Ajaev, V.S. & Homsy, G.M. 2006 Modeling shapes and dynamics of confined bubbles. *Annu. Rev. Fluid Mech.* **38** (1), 277–307.

Angelo, J.B., Lightfoot, E.N. & Howard, D.W. 1966 Generalization of the penetration theory for surface stretch: application to forming and oscillating drops. *AIChE J.* **12** (4), 751–760.

Aris, R. 1956 On the dispersion of a solute in a fluid flowing through a tube. *Proc. R. Soc. Lond.* A **235** (1200), 67–77.

Atasi, O., Khodaparast, S., Scheid, B. & Stone, H.A. 2017 Effect of buoyancy on the motion of long bubbles in horizontal tubes. *Phys. Rev. Fluids* **2**, 094304.

Auriault, J.L. & Adler, P.M. 1995 Taylor dispersion in porous media: analysis by multiple scale expansions. *Adv. Water Resour.* **18** (4), 217–226.

Auriault, J.-L. 2002 Upscaling heterogeneous media by asymptotic expansions. *J. Engng Mech. ASCE* **128** (8), 817–822.

Aussillous, P. & Quéré, D. 2000 Quick deposition of a fluid on the wall of a tube. *Phys. Fluids* **12** (10), 2367–2371.

BALESTRA, G., ZHU, L. & GALLAIRE, F. 2018 Viscous taylor droplets in axisymmetric and planar tubes: from Bretherton's theory to empirical models. *Microfluid Nanofluid* **22**, 67.
BARAK, M. & YESHAYAHU, K. 2005 Microbubbles. *CHEST* **128** (4), 2918–2932.
BATTIATO, I. & TARTAKOVSKY, D.M. 2011 Applicability regimes for macroscopic models of reactive transport in porous media. *J. Contam. Hydrol.* **120–121**, 18–26.
BEEK, W.J. & KRAMERS, H. 1962 Mass transfer with a change in interfacial area. *Chem. Engng Sci.* **17** (11), 909–921.
BENSOUSSAN, A., LIONS, J.L. & PAPANICOLAOU, G. 2011 *Asymptotic Analysis for Periodic Structures*. American Mathematical Society.
BERG, M., DAVIT, Y., QUINTARD, M. & LORTHOIS, S. 2020 Modelling solute transport in the brain microcirculation: is it really well mixed inside the blood vessels? *J. Fluid Mech.* **884**, A39.
BOURBATACHE, M.K., MILLET, O. & MOYNE, C. 2020 Upscaling diffusion–reaction in porous media. *Acta Mechanica* **38** (4), 1262–1287.
BOUTIN, C., AURIAULT, J.L. & GEINDREAU, C. 2010 *Homogenization of Coupled Phenomena in Heterogenous Media*. Wiley.
BRENNER, H. & STEWARTSON, K. 1980 Dispersion resulting from flow through spatially periodic porous media. *Phil. Trans. R. Soc. Lond.* A **297** (1430), 81–133.
BRETHERTON, F.P. 1961 The motion of long bubbles in tubes. *J. Fluid Mech.* **10** (2), 166–188.
BULL, J.L. 2005 Cardiovascular bubble dynamics. *Crit. Rev. Biomed. Engng* **33** (4), 299–346.
CHEN, J.-D. 1986 Measuring the film thickness surrounding a bubble inside a capillary. *J. Colloid Interface Sci.* **109** (2), 341–349.
COX, B.G. 1962 On driving a viscous fluid out of a tube. *J. Fluid Mech.* **14** (1), 81–96.
CUBAUD, T., SAUZADE, M. & SUN, R. 2012 CO_2 dissolution in water using long serpentine microchannels. *Biomicrofluidics* **6** (2), 022002.
ECKMANN, D.M. & LOMIVOROTOV, V.N. 2003 Microvascular gas embolization clearance following perfluorocarbon administration. *J. Appl. Physiol.* **94** (3), 860–868.
EGGERS, J. & FONTELOS, M.A. 2015 *Singularities: Formation, Structure, and Propagation*. Cambridge Texts in Applied Mathematics. Cambridge University Press.
FAIRBROTHER, F. & STUBBS, A.E. 1935 Studies in electro-endosmosis. Part VI. The 'bubble-tube' method of measurement. *J. Chem. Soc.* **1**, 527–529.
GANAPATHY, H., AL-HAJRI, E. & OHADI, M. 2013 Mass transfer characteristics of gas–liquid absorption during taylor flow in mini/microchannel reactors. *Chem. Engng Sci.* **101**, 69–80.
GANAPATHY, H., SHOOSHTARI, A., DESSIATOUN, S., ALSHEHHI, M. & OHADI, M. 2014 Fluid flow and mass transfer characteristics of enhanced CO_2 capture in a minichannel reactor. *Appl. Energy* **119**, 43–56.
DE GENNES, P.G., BROCHARD-WYART, F. & QUÉRÉ, D. 2003 *Capillarity and Wetting Phenomena: Drops, Bubbles, Pearls, Waves*. Springer.
GINLEY, G.M. & RADKE, C.J. 1988 Influence of surfactants on the flow of long bubbles through cylindrical capillaries. American Chemical Society, Division of Petroleum Chemistry, Preprints 33.
GROTBERG, J.B. 1994 Pulmonary flow and transport phenomena. *Annu. Rev. Fluid Mech.* **26** (1), 529–571.
GUPTA, P.S., GUPTA, A.S. & TAYLOR, G.I. 1972 Effect of homogeneous and heterogeneous reactions on the dispersion of a solute in the laminar flow between two plates. *Proc. R. Soc. Lond.* A **330** (1580), 59–63.
HAYASHI, K., HOSODA, S., TRYGGVASON, G. & TOMIYAMA, A. 2014 Effects of shape oscillation on mass transfer from a taylor bubble. *Intl J. Multiphase Flow* **58**, 236–245.
HEIL, M. 2001 Finite Reynolds number effects in the Bretherton problem. *Phys. Fluids* **13** (9), 2517–2521.
HIRASAKI, G.J. & LAWSON, J.B. 1985 Mechanisms of foam flow in porous media: apparent viscosity in smooth capillaries. *Soc. Petrol. Engng J.* **25** (02), 176–190.
HODGES, S.R., JENSEN, O.E. & RALLINSON, J.M. 2004 The motion of a viscous drop through a cylindrical tube. *J. Fluid Mech.* **501**, 279–301.
HORI, Y., BOTHE, D., HAYASHI, K., HOSOKAWA, S. & TOMIYAMA, A. 2020 Mass transfer from single carbon-dioxide bubbles in surfactant-electrolyte mixed aqueous solutions in vertical pipes. *Intl J. Multiphase Flow* **124**, 103207.
HORNUNG, U. 1997 *Homogenization and Porous Media*. Springer.
JIA, H.W. & ZHANG, P. 2016 Investigation of the taylor bubble under the effect of dissolution in microchannel. *Chem. Engng J.* **285**, 252–263.
KASTENS, S., HOSODA, S., SCHLÜTER, M. & TOMIYAMA, A. 2015 Mass transfer from single taylor bubbles in minichannels. *Chem. Engng Technol.* **38** (11), 1925–1932.
KHODAPARAST, S., KIM, M.K., SILPE, J.E. & STONE, H.A. 2017 Bubble-driven detachment of bacteria from confined microgeometries. *Environ. Sci. Technol.* **51** (3), 1340–1347.

KHODAPARAST, S., MAGNINI, M., BORHANI, N. & THOME, J.R. 2015 Dynamics of isolated confined air bubbles in liquid flows through circular microchannels: an experimental and numerical study. *Microfluid Nanofluid* **19**, 209–234.

LAMSTAES, C. & EGGERS, J. 2017 Arrested bubble rise in a narrow tube. *J. Stat. Phys.* **167**, 656–682.

LEUNG, S.S.Y., GUPTA, R., FLETCHER, D.F. & HAYNES, B.S. 2012 Gravitational effect on Taylor flow in horizontal microchannels. *Chem. Engng Sci.* **69** (1), 553–564.

LI, Y., GARING, C. & BENSON, S.M. 2020 A continuum-scale representation of Ostwald ripening in heterogeneous porous media. *J. Fluid Mech.* **889**, A14.

LI, Z., LI, G., LI, Y., CHEN, Y., LI, J. & CHEN, H. 2021 Flow field around bubbles on formation of air embolism in small vessels. *Proc. Natl Acad. Sci. USA* **118** (26), e2025406118.

LYNN, A.S. 2016 Droplets and bubbles in microfluidic devices. *Annu. Rev. Fluid Mech.* **48** (1), 285–309.

MAGNINI, M., FERRARI, A., THOME, J.R. & STONE, H.A. 2017 Undulations on the surface of elongated bubbles in confined gas-liquid flows. *Phys. Rev. Fluids* **2**, 084001.

MAURI, R. 1991 Dispersion, convection, and reaction in porous media. *Phys. Fluids* A **3** (5), 743–756.

MICHELIN, S., GUÉRIN, E. & LAUGA, E. 2018 Collective dissolution of microbubbles. *Phys. Rev. Fluids* **3**, 043601.

MIKELIĆ, A., DEVIGNE, V. & VAN DUIJN, C.J. 2006 Rigorous upscaling of the reactive flow through a pore, under dominant Péclet and Damkohler numbers. *SIAM J. Math. Anal.* **38** (4), 1262–1287.

NG, C.-O. 2006 Dispersion in steady and oscillatory flows through a tube with reversible and irreversible wall reactions. *Proc. R. Soc. Lond.* A **462** (2066), 481–515.

OLGAC, U. & MURADOGLU, M. 2013 Effects of surfactant on liquid film thickness in the Bretherton problem. *Intl J. Multiphase Flow* **48**, 58–70.

PARK, C.-W. 1992 Influence of soluble surfactants on the motion of a finite bubble in a capillary tube. *Phys. Fluids* A **4** (11), 2335–2347.

PARMIGIANI, A., HUBER, C., BACHMANN, O. & CHOPARD, B. 2011 Pore-scale mass and reactant transport in multiphase porous media flows. *J. Fluid Mech.* **686**, 40–76.

PICCHI, D. & BATTIATO, I. 2018 The impact of pore-scale flow regimes on upscaling of immiscible two-phase flow in porous media. *Water Resour. Res.* **54** (9), 6683–6707.

PICCHI, D., ULLMANN, A., BRAUNER, N. & POESIO, P. 2021 Motion of a confined bubble in a shear-thinning liquid. *J. Fluid Mech.* **918**, A7.

RATHNAWEERA, T.D., RANJITH, P.G. & PERERA, M.S.A. 2016 Experimental investigation of geochemical and mineralogical effects of CO_2 sequestration on flow characteristics of reservoir rock in deep saline aquifers. *Sci. Rep.* **6**, 19362.

RATULOWSKI, J. & CHANG, H.-C. 1990 Marangoni effects of trace impurities on the motion of long gas bubbles in capillaries. *J. Fluid Mech.* **210**, 303–328.

REINELT, D.A. & SAFFMAN, P.G. 1985 The penetration of a finger into a viscous fluid in a channel and tube. *SIAM J. Sci. Stat. Comput.* **6** (3), 542–561.

RIVERO-RODRIGUEZ, J. & SCHEID, B. 2019 Mass transfer around bubbles flowing in cylindrical microchannels. *J. Fluid Mech.* **869**, 110–142.

RUBINSTEIN, J. & MAURI, R. 1986 Dispersion and convection in periodic porous media. *SIAM J. Appl. Maths* **46** (6), 1018–1023.

DE RYCK, A. 2002 The effect of weak inertia on the emptying of a tube. *Phys. Fluids* **14** (7), 2102–2108.

SANKARASUBRAMANIAN, R., GILL, W.N. & BENJAMIN, T.B. 1973 Unsteady convective diffusion with interphase mass transfer. *Proc. R. Soc. Lond.* A **333** (1592), 115–132.

SCHWARTZ, L.W., PRINCEN, H.M. & KISS, A.D. 1986 On the motion of bubbles in capillary tubes. *J. Fluid Mech.* **172**, 259–275.

SHAO, N., GAVRIILIDIS, A. & ANGELI, P. 2010 Mass transfer during Taylor flow in microchannels with and without chemical reaction. *Chem. Engng J.* **160** (3), 873–881, 10th International Conference on Microreaction Technology.

SHIM, S., WAN, J., HILGENFELDT, S., PANCHAL, P.D. & STONE, H.A. 2014 Dissolution without disappearing: multicomponent gas exchange for CO_2 bubbles in a microfluidic channel. *Lab on a Chip* **14**, 2428–2436.

SHUKLA, I., KOFMAN, N., BALESTRA, G., ZHU, L. & GALLAIRE, F. 2019 Film thickness distribution in gravity-driven pancake-shaped droplets rising in a Hele-Shaw cell. *J. Fluid Mech.* **874**, 1021–1040.

SILVA, M.C.F., CAMPOS, J.B.L.M. & ARAÚJO, J.D.P. 2019 Mass transfer from a soluble wall into gas-liquid slug flow in a capillary tube. *Intl J. Heat Mass Transfer* **132**, 745–761.

SOBIESZUK, P., POHORECKI, R., CYGAŃSKI, P. & GRZELKA, J. 2011 Determination of the interfacial area and mass transfer coefficients in the Taylor gas–liquid flow in a microchannel. *Chem. Engng Sci.* **66** (23), 6048–6056.

SOULAINE, C., ROMAN, S., KOVSCEK, A. & TCHELEPI, H.A. 2018 Pore-scale modelling of multiphase reactive flow: application to mineral dissolution with production of CO_2. *J. Fluid Mech.* **855**, 616–645.

STEBE, K.J. & BARTHÉS-BIESEL, D. 1995 Marangoni effects of adsorption–desorption controlled surfactants on the leading end of an infinitely long bubble in a capillary. *J. Fluid Mech.* **286**, 25–48.

STEEFEL, C.I., MOLINS, S. & TREBOTICH, D. 2013 Pore scale processes associated with subsurface CO_2 injection and sequestration. *Rev. Mineral. Geochem.* **77** (1), 259–303.

STONE, H.A. 2010 Interfaces: in fluid mechanics and across disciplines. *J. Fluid Mech.* **645**, 1–25.

SUZUKI, A. & ECKMAN, D.M. 2003 Embolism bubble adhesion force in excised perfused microvessels. *Anesthesiology* **99**, 400–408.

SVETLOV, S.D. & ABIEV, R.SH. 2016 Modeling mass transfer in a Taylor flow regime through microchannels using a three-layer model. *Theor. Found. Chem. Engng* **50**, 975–989.

TAYLOR, G.I. 1953 Dispersion of soluble matter in solvent flowing slowly through a tube. *Proc. R. Soc. Lond.* A **219** (1137), 186–203.

TAYLOR, G.I. 1961 Deposition of a viscous fluid on the wall of a tube. *J. Fluid Mech.* **10** (2), 161–165.

VADAPALLI, A., GOLDMAN, D. & POPEL, A.S. 2002 Calculations of oxygen transport by red blood cells and hemoglobin solutions in capillaries. *Artif. Cells Blood Substit. Biotechnol.* **30** (3), 157–188.

YU, Y.E., KHODAPARAST, S. & STONE, H.A. 2017 Armoring confined bubbles in the flow of colloidal suspensions. *Soft Matt.* **13**, 2857–2865.

YU, Y.E., ZHU, L., SHIM, S., EGGERS, J. & STONE, H.A. 2018 Time-dependent motion of a confined bubble in a tube: transition between two steady states. *J. Fluid Mech.* **857**, R4.

YUE, J., LUO, L., GONTHIER, Y., CHEN, G. & YUAN, Q. 2009 An experimental study of air–water Taylor flow and mass transfer inside square microchannels. *Chem. Engng Sci.* **64** (16), 3697–3708.

ZHOU, Y., YAO, C., ZHANG, P., ZHANG, X., LÜ, H. & ZHAO, Y. 2020 Dynamic coupling of mass transfer and chemical reaction for Taylor flow along a serpentine microchannel. *Ind. Engng Chem. Res.* **59** (19), 9279–9292.

ZHU, C., LU, Y., FU, T., MA, Y. & LI, H.Z. 2017 Experimental investigation on gas-liquid mass transfer with fast chemical reaction in microchannel. *Intl J. Heat Mass Transfer* **114**, 83–89.